Journal Pre-proofs

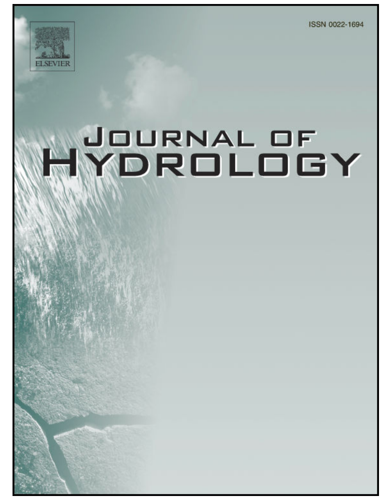

Research papers

Climate change effects on rainfall extreme value distribution: The role of skewness

Davide Luciano De Luca, Elena Ridolfi, Fabio Russo, Benedetta Moccia, Francesco Napolitano

PII: S0022-1694(24)00352-4
DOI: https://doi.org/10.1016/j.jhydrol.2024.130958
Reference: HYDROL 130958

To appear in: *Journal of Hydrology*

Received Date: 4 April 2023
Revised Date: 21 January 2024
Accepted Date: 9 February 2024

Please cite this article as: Luciano De Luca, D., Ridolfi, E., Russo, F., Moccia, B., Napolitano, F., Climate change effects on rainfall extreme value distribution: The role of skewness, *Journal of Hydrology* (2024), doi: https://doi.org/10.1016/j.jhydrol.2024.130958

CLIMATE CHANGE EFFECTS ON RAINFALL EXTREME VALUE DISTRIBUTION: THE ROLE OF SKEWNESS

Davide Luciano De Luca[1], Elena Ridolfi[1], Fabio Russo[1], Benedetta Moccia[1], Francesco Napolitano[1]

[1]Department of Civil, Building and Environmental Engineering Sapienza University of Rome, Italy

Corresponding author: Davide Luciano De Luca, davide.deluca@unical.it

Abstract

Quantifying the potential effects of Climate Change (CC) on hydrological scales is a topic with a more and more increasing interest for the scientific community, given the CC impact on agriculture, industry, economy, human health, ecosystems, among the others. In this context, the paper focuses on the sub-daily Annual Maxima (AM) of rainfall height time series, and specifically on the crucial role played by initial skewness, i.e. the skewness of the observed rainfall series used to evaluate potential parametric trends. Here a quick and user-friendly methodology is proposed, that is aimed at quantifying plausible future changes in terms of probability distributions assumed at rain gauge scale, from projections of any climatic model. In detail, the Generalized Extreme Value (GEV) and the Two-Component Extreme Value (TCEV) distributions are adopted as probability functions suitable for modelling observed rainfall AM series, which could increase their frequency and magnitude into future horizons under CC. EURO-CORDEX projections for Europe are considered, under the hypothesis that the values of the change factor, i.e. the ratio between the values of a specific quantile at two specific time horizons, are invariant when moving from an areally-averaged scale (typical for any climate model) to a point rain gauge scale, which induces that future changes are provided (in terms of frequency and magnitude of extreme events) without the need of any spatial downscaling from the assumed projections. The proposed methodology can contribute to hazard quantification associated to potential climate changes, and thus it can play a crucial role in the assessment of hydraulic structures resilience; the obtained results, specific for the study area of Italy, but easily extendable on a global scale, showed that larger increases in frequency of future heavy events are expected for time series with "EV1 alike" values of initial skewness.

Keywords: rainfall annual maxima; TCEV distributions; skewness, climate change, extreme value distributions

1. Introduction

Evaluation of Climate Change (CC) effects on a wide variety of contexts (e.g. agriculture, industry, economy, human health, and ecosystems) and, consequently, Climate Change Adaptation (CCA) and Disaster Risk Reduction (DRR) strategies clearly constitute key topics for the scientific community, in order to build more resilient societies in terms of structures, infrastructures, and people awareness, among the others. As regards hydraulic and geological risks, heavy rainfall events are the main precursor for floods and landslides, and then their potential increase in frequency and/or in magnitude can induce a higher occurrence of these disastrous phenomena, thus making necessary an adequate mitigation design, which may involve structural and/or non-structural measures.

In this context, focusing on the daily scale, Papalexiou and Montanari (2019) performed a world-wide analysis of 8730 precipitation time series recorded in the 1964-2013 period; they found global and zonal increasing trends in the frequency of extremes, while changes in magnitude are not so evident.

Nowadays, a similar world-wide analysis is difficult to carry out for sub-daily rainfall scales, which are of main interest for the analysis of flash floods and shallow landslides, due to a scarce availability of long time series in many parts of the globe (see, for example, Fig. 1 in Fowler et al., 2021). However, even if the sample size of high-resolution rainfall series is long enough, the obtained trends from observed data could not be suitable for projection into the future, for two main reasons (Blöschl et al., 2019): first, the trends could be related to climate variability and not to persistent changes in time; second, the trend of a series depends on the observation period, so the outcome could be different if the observation period is extended.

To overcome these issues, climate projections from General Circulation Models (GCMs,Butcher and Zi, 2019; Chandra et al., 2015; Khazaei, 2021; Lima et al., 2016; Ragno et al. 2018), Regional Climate Models (RCMs, Fadhel et al., 2017; Fluixá-Sanmartín et al., 2019; Forestieri et al., 2018a; Ganguli and Coulibaly, 2019) and Convention Permitting Models (CPMs) are usually adopted (Kendon et al., 2021; Vergara-Temprado et al., 2021).

However, it should be highlighted that outputs from all these three classes of models are affected by relevant uncertainties or high computational costs for applications at hydrological scales (Kourtis and Tsihrintzis, 2021, 2022). In fact, the spatiotemporal resolutions of GCMs are too coarse, thus requiring dynamic or statistical downscaling (Themeßl et al., 2012; Kourtis and Tsihrintzis, 2021). With a dynamic downscaling, RCMs are forced by GCMs under different climate scenarios (i.e., Representative Concentration Pathways – RCPs or Special Report on Emissions Scenarios-SRES). RCMs are however unsuitable to accurately represent convective storms (Berg et al., 2013, 2019) affecting sub-daily scales, and then further spatial and temporal downscaling should be necessary. Nevertheless, statistical downscaling techniques should be adopted with caution (Kourtis and Tsihrintzis, 2021), as they represent a further source of uncertainty, and they are sensitive to the time period for which they are calibrated. CPMs run with a horizontal resolution less than 4 km, and are able to better simulate hourly and sub-hourly rainfall extremes (Vergara-Temprado et al., 2021) due to their explicit representation of convection (Ban et al., 2020; Ban et al., 2014; Kendon et al., 2012). However, they suffer from biases, and bias correction is suggested before performing an extreme value analysis (Kendon et al., 2014; Berthou et al., 2020). Moreover, CPMs require high computational costs (Kendon et al., 2021), which limit their use only for small regions and for short reference periods (e.g., 10–20 years).

Although all these mentioned critical aspects, literature contains many papers in which a joint use of observed sub-daily series and climate models is proposed to evaluate possible CC effects on extremes at hydrological scales (e.g.Ganguli and Coulibaly, 2017; Hassanzadeh et al., 2014; Kao and Ganguly, 2011; Kuo et al., 2015; Mailhot et al., 2007; Mirhosseini at al., 2013; Shahabul Alam and Elshorbagy, 2015; Simonovic et al., 2016). The reader can find an extensive review in Lanciotti et al. (2022) and Sandink et al. (2016). In particular, we can mention the worldwide INTENSE Project (INTElligent use of climate models for adaptation to non-Stationary hydrological Extremes, Blenkinsop et al., 2018) and the work of Hosseinzadehtalaei et al. (2020) focusing on Europe and showing that larger changes are expected for longer return periods and shorter durations.

In this context of relevant uncertainties about output from GCMs, RCMs and CPMs, many governmental agencies did not adopt these projections to take into account the future climate, but implemented simple adaptation strategies for the modification of rainfall Intensity-Duration-Frequency (IDF) and Amount-Duration-Frequency (ADF) curves , which constitute the most used input for the design of several water infrastructures (Martel et al., 2021). For instance, Belgium and the UK, respectively, apply an increase of 30% (Madsen et al., 2014; Willems, 2011) and 20% (UK Department for Infrastructure, 2020) on all rainfall extremes. In Canada, a similar approach is adopted in the Province of Quebec (18%; MDDELCC, 2017) and in the City of Moncton, New Brunswick (20%; EPWDR, 2011). Denmark considers different safety factors, based on the return period (i.e., 20%, 30%, and 40% increases are added to the 2-, 10-, and 100-year return periods, respectively). The Swedish Water and Wastewater Association (Madsen et al., 2014; Svenskt Vatten, 2011) recommends a fixed percentage increase, with an adaptive variation between 5% and 30%, depending on the region. More “physically-based” approaches refers to the well-known Clausius-Clapeyron relationship (Westra et al., 2014), according to which there should be an increase of approximately 7% in rainfall depth per 1°C of warming (projected by climate models), even if this scaling can depend on rainfall extremes frequency, i.e. longer return period events can be characterized by larger increases, leading to a super (i.e. twice) Clausius-Clapeyron scaling in some cases. For instance, the Australian Rainfall-Runoff guidelines (ARR; Ball et al., 2019) recommends a 5% increase per degree Celsius of warming while the Canadian Standard Association (CSA, 2019) recommends a value of approximately 7%/°C. However, the CSA (2019) acknowledges that shorter duration events could follow a super Clausius-Clapeyron relationship, implying that a larger rate than approximately 7%/°C of warming may be applied, depending on the area. The super Clausius-Clapeyron relationship, inducing larger increases for longer return periods and shorter durations, clearly justified the previously mentioned results for Europe, obtained by Hosseinzadehtalaei et al. (2020).

Moreover, focusing on the concept of return period, Cooley (2013) highlighted that it becomes ambiguous when moving from stationary to nonstationary conditions. However, the return period can still be defined for operational purposes at least in two ways: i) the extension to nonstationary conditions of the concept of expected occurrence interval, i.e. the expected waiting time until an exceedance occurs (Salas and Obeysekera, 2014); ii) the T-year period in which the expected number of exceedances, related to an associated design value, is equal to one (Parey et al., 2007, 2010). Regardless of its definition, the return period exactly or approximately summarizes the average annual probability of an exceedance. Specifically for Annual Maxima (AM) rainfall time series, the previously mentioned second definition implies:

$$T(x) = \frac{1}{1 - \frac{1}{T}\sum_{i=1}^{T} F_{X,i}(x)} \tag{1}$$

which must be numerically solved for any assigned value x of the random variable X; $F_{X,i}(x)$ represents the Cumulative Density Function (CDF), assumed as a variable in each i-th year, for AM distributions. Obviously, under stationary conditions, Eq. (1) simplifies in the well-known expression:

$$T(x) = \frac{1}{1 - F_X(x)} \tag{2}$$

From Eq. (1), it is clear that, under nonstationary conditions, the concept of the T-year design value is not easily associated to the F-quantile, i.e. there is not a “one to one” correspondence $T(x)$-$F_X(x)$ like in Eq. (2), where stationarity is supposed. By analyzing the denominator in Eq.(1), evaluation of $T(x)$ associated to a specific design value x depends on a summation of $F_{X,i}(x)$ (with i = 1, … T), which in turn depends on when this T-year window begins: for example, the temporal intervals [2001;2030] and [2021; 2050] can provide two different 30-year design values, because $F_{X,i}(x)$ can assume diverse values in these two different 30-year windows. Moreover, the mathematical structure (linear, non-linear, step, etc.) of the assumed/hypothesized parametric trend along a prefixed T-year period also influences the result of Eq. (1). Instead, in some papers the correspondence $T(x)$-$F_X(x)$ is carried out by using Eq. (2) even in nonstationary conditions, though this approach appears less rigorous. To maintain precision in our work, we will exclusively consider variations in terms of F-quantile, unless other computational cues are provided.

Building upon from the above discussed overview on adaptation strategies, our work introduces a novel and efficient methodology. This approach is rooted in the hypothesis that the values of change factor, i.e. the ratio between the values of a specific quantile at two specific time horizons, are invariant when moving from an areally-averaged scale (typical for any climate model) to a point rain gauge scale (Kilsby et al., 2007; Onof and Arnbjerg-Nielsen, 2009). The significance of our proposed methodology lies in its ability to quantify (starting from projections of any climatic model) possible future changes in probability distributions at rain gauge scale without any spatial downscaling of climate models projections. It enables the assessment of mean frequency and magnitude of extreme events and thus of any quantile, providing a valuable tool for hazard assessment over predetermined temporal horizons relevant to the design life periods of structures.

To assess the impacts of CC on extreme values distributions in terms of parameters variation, we focused on analysing the Generalized Extreme Value (GEV, Jenkinson, 1955) and the Two-Component Extreme Value (TCEV, Rossi et al., 1984) distributions. We choose these two for their suitability in modelling rainfall AM series, especially considering potential increases in frequency and magnitude under CC, based on EURO-CORDEX projections for Europe (Hosseinzadehtalaei et al., 2020). Although we tested the methodology using observed rainfall characteristics in Italy, its applicability extends globally. We posit that our methodology holds particular relevance in the context of evaluating the resilience of hydraulic structures under CC, especially concerning hazard quantification.

2. Methodology

Focusing on rainfall AM modelling, the widely used functions in literature are EV1 (Gumbel, 1958), GEV (Generalized Extreme Value, Jenkinson, 1955), TCEV (Two Component Extreme Value, Rossi et al., 1984), Log Pearson type III (Bobee, 1975), the 3-parameter LogNormal (Johnson et al., 1994, pp. 208–238), the generalized Pareto (Hosking and Wallis, 1987; Johnson et al., 1994, p. 615), the generalized Logistic (Balakrishnan and Leung, 1988). Moreover, other distributions were recently proposed; among them we can mention: i) the Burr XII type (Moccia et al., 2021); ii) probability functions which are based on non-asymptotic approach (Marani and Ignaccolo, 2015, Lombardo et al., 2019). Another way for statistical modelling of extreme values is constituted by the Peaks Over a Threshold (POT) analysis (see Pan et al., 2022, for a very exhaustive review), in which all the extremes above a threshold are considered, and thus not only the maximum value of each year.

The AM modelling is the most popular approach in practice, given its straightforwardness in the sampling process. However, by applying the theorem of total probability, the well-known relationship among AM and POT series is obtained, from which the asymptotic extreme value theory is derived (Todorovic, 1970; De Michele, 2019):

$$F_X(x) = \sum_{n=0}^{+\infty} P_N(n)[F_{X,POT}(x)]^n \tag{3}$$

where $F_X(x) = P[X \leq x]$ is the CDF for AM distribution, $P_N(n)$ represents the probability associated to n exceedances (assumed as independent among them) of the threshold in one year and $F_{X,POT}(x)$ is the CDF for the peaks associated to the exceedances. Consequently, from Eq. (3) it is possible to obtain several expressions for $F_X(x)$, depending on the specific adopted mathematical formulas for $P_N(n)$ and $F_{X,POT}(x)$. In this work, we adopted the following AM distributions for the development of the proposed methodology: GEV (Sect. 2.1), derived from a Poisson counting process for $P_N(n)$ and a Generalized Pareto distribution (Wang 1991) for $F_{X,POT}(x)$; TCEV (Sect. 2.2), obtained by assuming a Poisson counting process for $P_N(n)$ and a mixture of two exponential distributions for $F_{X,POT}(x)$.

Whatever is the mathematical expression for $F_X(x)$, it can be also indicated as $F_X\big(x,\underline{\Phi}(t)\big)$, where $\underline{\Phi}(t)$ is the array of parameters values at time t; it is clear that $\underline{\Phi}(.)$ is invariant in time if the model $F_X(x)$ is supposed as stationary. Starting from the chosen AM distributions, the proposed procedure considers the EURO-CORDEX projections for Europe (Hosseinzadehtalaei et al. 2020), because application regards Italy (Sect. 3); they can be summarized, for any investigated cell and sub-daily duration, with a plot like the one in Fig.1, where:

- $F = F_X(.)$ for a simpler notation;
- the indicator $I_F = \frac{1}{1-F}$ is represented on the horizontal axis. Although it has the same mathematical expression of Eq. (2), it is not a return period in the context of Climate Change, as discussed in the Introduction;
- the Change Factor $C(F) = \frac{X_F(t_2)}{X_F(t_1)}$ is represented on the vertical axis: it is defined as the ratio between the values of a quantile $X_F(.)$ at two specific times, t_2 and t_1, which represent the upper and lower bound, respectively, of a temporal horizon of interest. Clearly, $X_F(t_2)$ and $X_F(t_1)$ can be also indicated, in equivalent way, as $X_F\big(\underline{\Phi}(t_2)\big)$ and $X_F\big(\underline{\Phi}(t_1)\big)$, respectively;
- M and Q are the asymptotic and the intercept values of $C(F)$ when $I_F \rightarrow +\infty$ (i.e. $F \rightarrow 1$) and $I_F \rightarrow 1$ (i.e. $F \rightarrow 0$), respectively. In Fig.1, the represented condition $M > Q$ implies that larger quantiles present larger values of $C(F)$. Q is usually greater than 1, but $Q < 1$ could emerge in some cases. The presence of an asymptotic value when $F \rightarrow 1$ is also theoretically justified by analyzing GEV and TCEV distributions (see Eqs. 11a-b and Eqs. 22a-b).

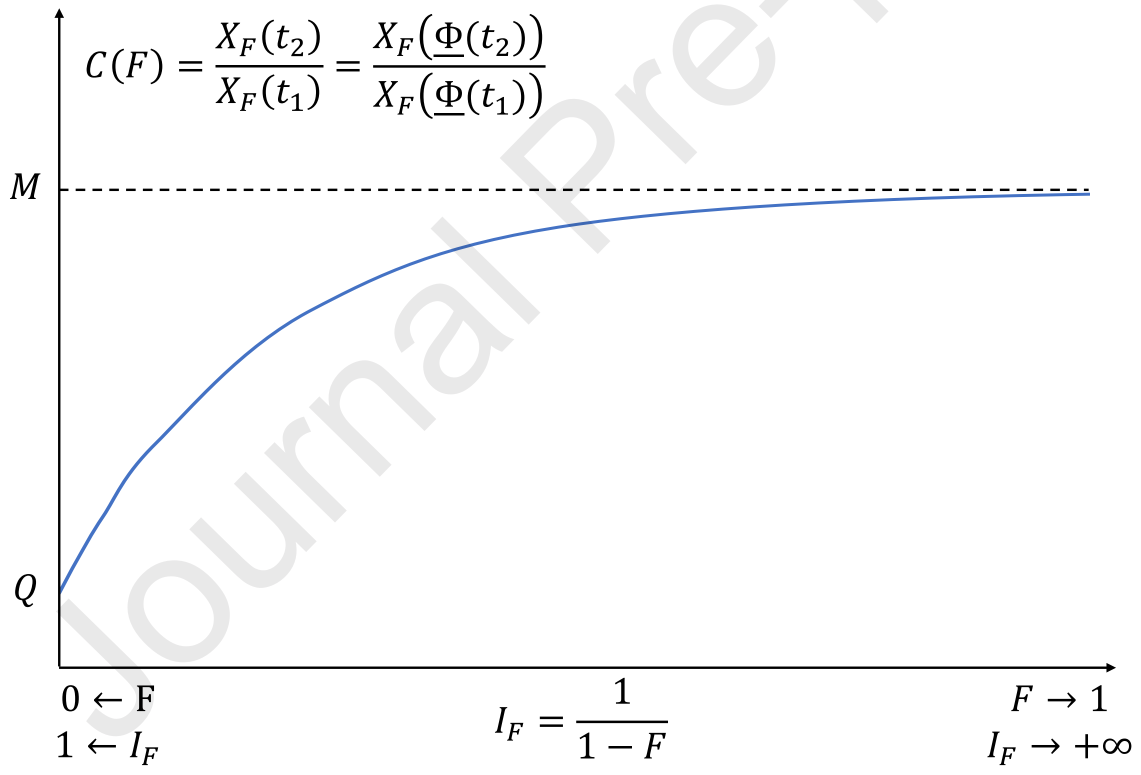

Figure 1. Plot of Change Factor $C(F)$, specific for any investigated cell and sub-daily duration (adapted from Hosseinzadehtalaei et al., 2020)

As already mentioned in the Introduction, the diagram $I_F - C(F)$ can be assumed as invariant passing from an areally-averaged scale (typical for any climate model) to the point rain gauge scale (Kilsby et al., 2007;

Onof and Arnbjerg-Nielsen, 2009), and then it can be used for evaluation of CC effects for point time series of interest.

Overall, the methodology can be schematized as reported in Fig. 2: for any spatial cell and sub-daily duration, the input quantities are the array $\underline{\Phi}(t_1)$ at time t_1, M and Q values, while the output is constituted by the array $\underline{\Phi}(t_2)$ at the final time t_2; the difference between the arrays $\underline{\Phi}(t_2)$ and $\underline{\Phi}(t_1)$ clearly helps to quantify the variations in terms of frequency and magnitude of extreme events (see Sect. 2.1, 2.2 and 3). Evaluation of $\underline{\Phi}(t_2)$ is carried out by simultaneously imposing:

$$M = \lim_{\substack{F\to 1 \\ (I_F\to +\infty)}} \frac{X_F(t_2)}{X_F(t_1)} = \lim_{\substack{F\to 1 \\ (I_F\to +\infty)}} \frac{X_F\left(\underline{\Phi}(t_2)\right)}{X_F\left(\underline{\Phi}(t_1)\right)} \tag{4a}$$

$$Q = \lim_{\substack{F\to 0 \\ (I_F\to 1)}} \frac{X_F(t_2)}{X_F(t_1)} = \lim_{\substack{F\to 0 \\ (I_F\to 1)}} \frac{X_F\left(\underline{\Phi}(t_2)\right)}{X_F\left(\underline{\Phi}(t_1)\right)} \tag{4b}$$

and the minimization of the objective function S, defined as:

$$S = \sum_{i=1}^{n_F} \frac{\left|C_{F_X}\left(F_i, \underline{\Phi}(t_1), \underline{\Phi}(t_2)\right) - C(F_i)\right|}{C(F_i)} \tag{4c}$$

where n_F is the number of considered frequencies F_i ($i =$ 1, …., n_F), $C(F_i)$ are the known change factor values from plots like Fig.1 (for any AM sub-daily duration and any cell of interest), while $C_{F_X}(F_i)$ are the change factors associated to the chosen $F_X(.)$ distribution, clearly depending on the arrays $\underline{\Phi}(t_1)$ and $\underline{\Phi}(t_2)$.

The whole work is aimed to investigate the eventual presence of statistical "drivers", which could induce different values for $\underline{\Phi}(t_2)$ (i.e., different variations of frequency and magnitude of extreme events) starting from assigned change factors. Sects. 2.1 and 2.2 detail the methodology for GEV and TCEV distributions, respectively, and highlight how TCEV should be preferred, as it is also able to discriminate ordinary and rarer extreme events. In this context, Sect. 3 focuses on the crucial role played by the skewness at t_1 of the time series, as a statistical driver.

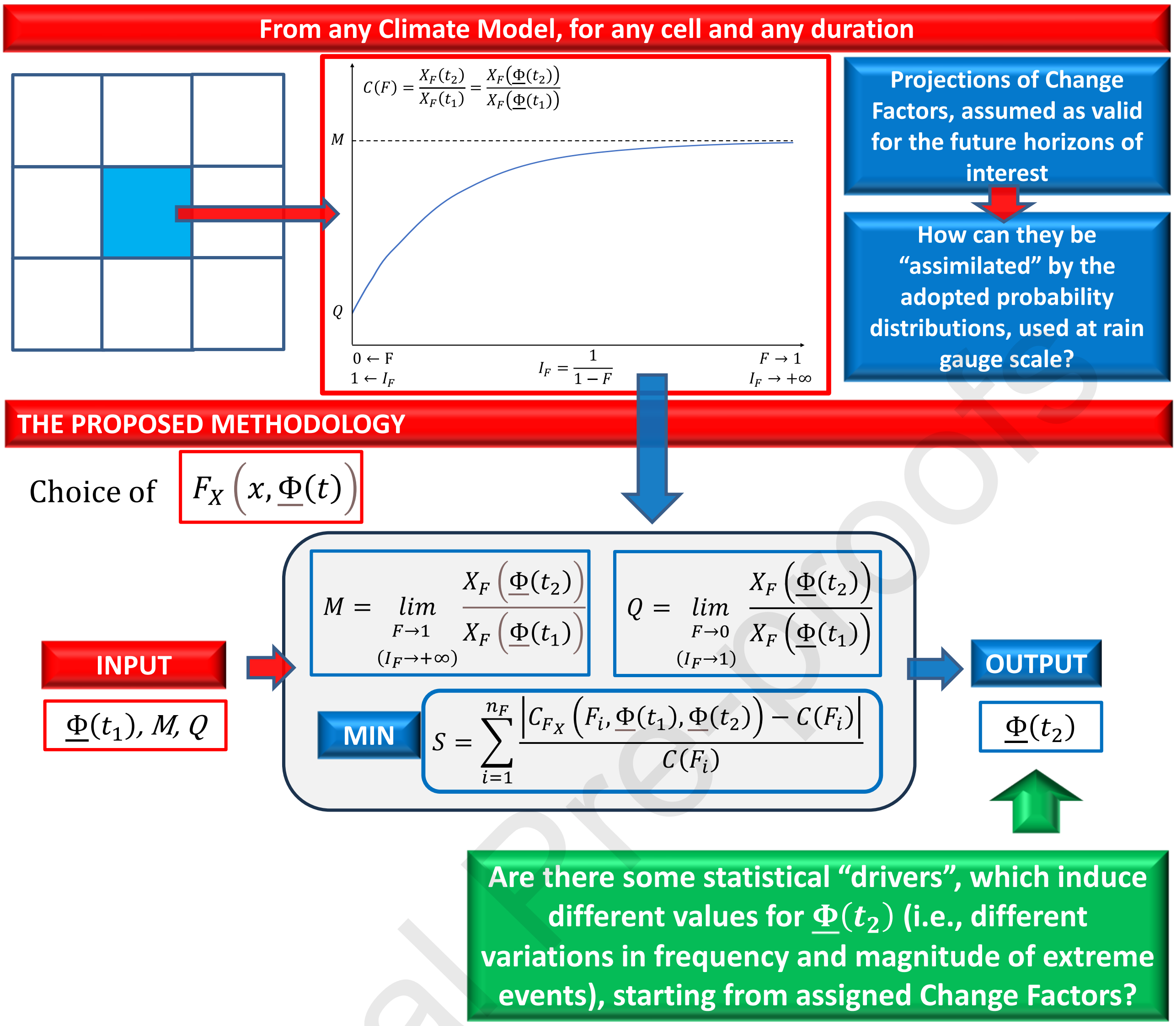

Figure 2. Overview of the proposed methodology.

2.1. Theoretical background for GEV distribution

The GEV distribution is characterized by the following CDF (Jenkinson, 1955; Coles, 2001):

$$F_X(x) = F_X(x, \underline{\Phi}) = \begin{cases} e^{-\left[1-b\left(\frac{x}{\theta}-\ln\Lambda\right)\right]^{1/b}} & b \neq 0 \\ e^{-e^{-\left(\frac{x}{\theta}-\ln\Lambda\right)}} & b = 0 \end{cases} \tag{5}$$

where Λ is related to the mean annual number of exceedances above a given threshold, θ is the scale parameter, b corresponds to the shape parameter and, clearly, $\underline{\Phi} = (\Lambda, \theta, b)$. When $b = 0$, the GEV distribution coincides with EV1 function (Gumbel, 1958). Moreover, EV2 (i.e. Frechet) and EV3 (i.e. Reversed Weibull) laws are obtained when $b < 0$ and $b > 0$, respectively (Singh, 1998). Fig. 3 shows examples of GEV functions for given b values on the EV1 probabilistic plot. It must be remarked that the k-th moment of the GEV distribution exists if $b > -1/k$; i.e., the mean exists if $b > -1$, the variance if $b > -1/2$, the skewness if $b > -1/3$ (Gupta, 2011).

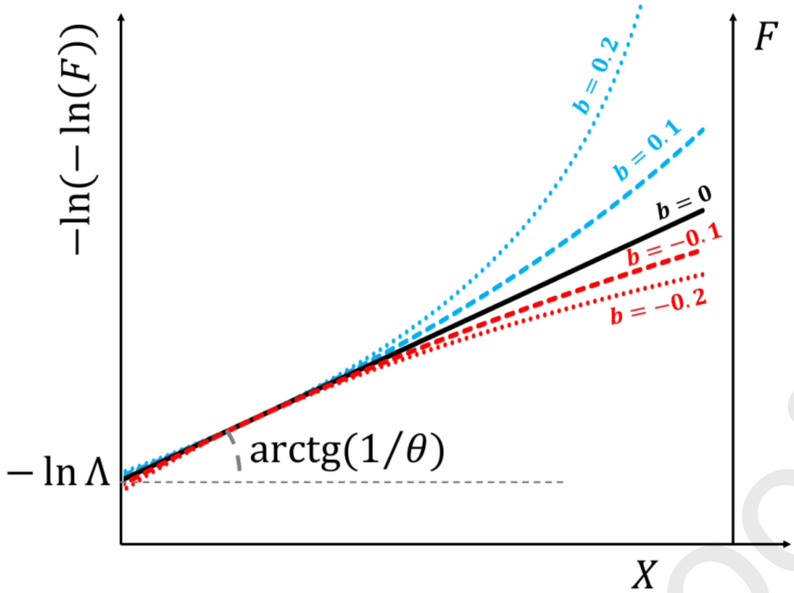

Figure 3. Examples of GEV functions for specific b values on the EV1 probabilistic plot. The slope angle $\mathrm{arctg}\,(1/\theta)$ and the intercept $-\ln\Lambda$ are related to the straight line associated to EV1 function, i.e. a GEV with $b = 0$.

Focusing on the theoretical skewness γ, its expression depends on the shape parameter b only (Gupta, 2011; Dey and Yan, 2016):

$$\gamma = \begin{cases} sgn(b) \cdot \dfrac{-\Gamma(1+3b) + 3\Gamma(1+2b)\cdot\Gamma(1+b) - 2\Gamma^3(1+b)}{[\Gamma(1+2b) - \Gamma^2(1+b)]^{1.5}} & b \neq 0 \\ 1.14 & b = 0 \end{cases} \tag{6}$$

where $sgn(.)$ and $\Gamma(.)$ are Sign and Complete Gamma functions, respectively (Abramowitz and Stegun, 1970). From Fig. 4, it can be highlighted that EV3 distribution is characterized by skewness values which are less than EV1 one, even negative in many cases. Consequently, as EV3 also presents a finite upper bound for X (Kottegoda and Rosso, 2008, p. 417; Moccia et al., 2021), this distribution has limited applications for analysis of hydrological AM series (Gupta, 2011). Therefore, in this work, authors only considered GEV functions with $b \leq 0$.

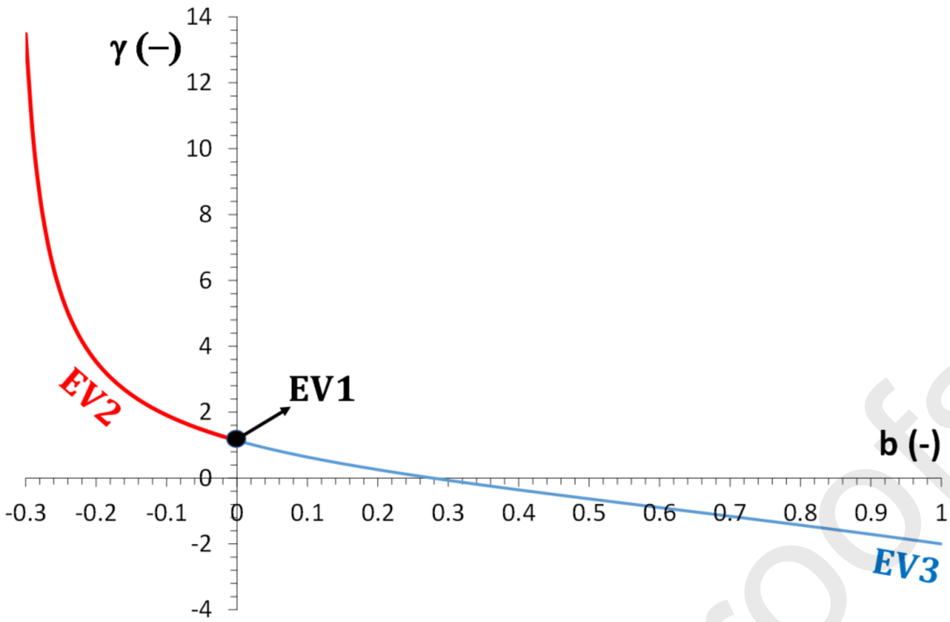

Figure 4. GEV skewness against the shape parameter b.

Eq. (5) can be rewritten in terms of the reduced and dimensionless variable $Y = \frac{X}{\theta} - ln\Lambda$ (Rossi et al., 1984):

$$F_Y(y) = \begin{cases} e^{-[1-by]^{1/b}} & b \neq 0 \\ e^{-e^{-y}} & b = 0 \end{cases} \tag{7}$$

As Y is a linear transformation of X, these two random variables clearly present the same value for skewness and $F_X(x) = F_Y(y)$. Eq. (7) obviously allows for a comparison, in terms of probability distribution, among samples with different scales θ and values of Λ. From Eq. (7), the expression for the generic quantile $Y_F = Y_F$ (b) is:

$$Y_F = \begin{cases} \dfrac{\left[1 - \left(-\ln F_Y(y)\right)^b\right]}{b} & b \neq 0 \\ -\ln[-\ln F_Y(y)] & b = 0 \end{cases} \tag{8}$$

with $Y_F(b) \to +\infty$ and $Y_F(b) \to -\infty$ when $F_Y(y) \to 1$ and $F_Y(y) \to 0$, respectively, for $b \leq 0$ (i.e. for EV1 and EV2 distributions, considered in this work). Then, X_F is computed as:

$$X_F = \theta \cdot (Y_F(b) + \ln\Lambda) \tag{9}$$

Eqs. (5-9) refer to the stationary approach (i.e., parameters are assumed as constant in time). As also indicated in Sect. 2, the extension to a nonstationary modelling implies to consider all, or some (at least one) parameters as varying with covariates, which could be time or explanatory variables that vary with time (Salas et al., 2018). Sometimes, both Λ and θ are assumed as $\Lambda(t)$ and $\theta(t)$, while keeping b constant (El Adlouni et al., 2007; Ruggiero et al., 2010). As reported in Coles (2001), for nonstationary (NS) GEV models it appears unrealistic to consider the shape parameter b as a smooth function of time or a function of a covariate, as it is difficult to estimate b with precision even in the stationary case.

In this context of invariance for shape parameter b, it is clear from Eqs. (7-8) that $F_Y(y)$ and, consequently, all the quantiles Y_F, can be modelled with a stationary approach, while the relative variation of the quantile X_F in the time interval $[t_1; t_2]$ can be computed as:

$$\frac{\Delta X_F(t_2-t_1)}{X_F(t_1)}=\frac{X_F(t_2)-X_F(t_1)}{X_F(t_1)}=C(F)-1= \tag{10a}$$
$$=\frac{\theta(t_2)\cdot(Y_F+\ln\Lambda(t_2))-\theta(t_1)\cdot(Y_F+\ln\Lambda(t_1))}{\theta(t_1)\cdot(Y_F+\ln\Lambda(t_1))}=\frac{\theta(t_2)\cdot(Y_F+\ln\Lambda(t_2))}{\theta(t_1)\cdot(Y_F+\ln\Lambda(t_1))}-1$$

in which, clearly, $Y_F=Y_F(b(t_2))=Y_F(b(t_1))=Y_F(b)$ for a prefixed value of shape parameter b assumed as constant in time. In this work, we set $\theta(t_2)=M\theta(t_1)$ and $\Lambda(t_2)=K\Lambda(t_1)$, where M and K are factors of increase/decrease. In this context, the use of the symbol "M" is not ambiguous with respect to Fig.1: as specified in Eqs. 11a-b, this factor of increase/decrease for θ corresponds to the asymptotic value of $C(F)$ when $F\to1$. Eq. (10a) can be rewritten as:

$$\frac{\Delta X_F(t_2-t_1)}{X_F(t_1)}=C(F)-1=\frac{M\cdot\theta(t_1)\cdot(Y_F+\ln K\Lambda(t_1))}{\theta(t_1)\cdot(Y_F+\ln\Lambda(t_1))}-1=\frac{M\cdot(Y_F+\ln K\Lambda(t_1))}{(Y_F+\ln\Lambda(t_1))}-1 \tag{10b}$$

Figs. (5-6) illustrate the values assumed by $\Delta X_F/X_F$ for several initial values (i.e. at t_1) of Λ and F = 0.5, 0.9, 0.98, 0.995, when $b\ =\ 0$ (EV1) and $b=-0.1$ and -0.2 (EV2), and by considering $M\ =\ 1$, 1.2, 1.3 and K varying from 0.5 to 3. For each value of shape parameter b and for any initial value of Λ, a reader can observe a clockwise rotation of the $\Delta X_F/X_F$ curve when F increases, with respect to the center placed in the point (K = 1, $\Delta X_F/X_F=M-1$); this rotation tends to the horizontal line having equation $\Delta X_F/X_F=M-1$, as below demonstrated by evaluating the limit of Eq. (11) when $F\to1$ (i.e., $Y_F\to+\infty$):

$$\lim_{\substack{F\to1\\(Y_F\to+\infty)}}\frac{M\cdot(Y_F+\ln K\Lambda(t_1))}{(Y_F+\ln\Lambda(t_1))}-1\ =\ \lim_{\substack{F\to1\\(Y_F\to+\infty)}}\frac{Y_F\cdot M\cdot\left(1+\frac{\ln K\Lambda(t_1)}{Y_F}\right)}{Y_F\cdot\left(1+\frac{\ln\Lambda(t_1)}{Y_F}\right)}-1\ =M-1 \tag{11a}$$

from which it is straightforward to assert that (as also expected from Eq. 4a):

$$\lim_{\substack{F\to1\\(Y_F\to+\infty)}}C(F)\ =\ \lim_{\substack{F\to1\\(Y_F\to+\infty)}}\frac{Y_F\cdot M\cdot\left(1+\frac{\ln K\Lambda(t_1)}{Y_F}\right)}{Y_F\cdot\left(1+\frac{\ln\Lambda(t_1)}{Y_F}\right)}=M \tag{11b}$$

Consequently, it is evident that, by hypothesizing the shape parameter b as invariant, longer quantiles present larger increases of $\Delta X_F/X_F$ when $K\leq1$ (i.e., a decrease of the mean annual number Λ of events above a threshold), and smaller increase of $\Delta X_F/X_F$ for $K>1$. Focusing the investigation on Europe, the case $K\leq1$ well-matches with Hosseinzadehtalaei et al. (2020), in terms of greater $\Delta X_F/X_F$ values for higher percentiles, and it is clearly compatible with the expected longer dry spells of climatic projections

(Seneviratne et al., 2012; Hov et al., 2013). Specifically, the ranges [0.75; 1] for K and [1.2; 1.3] for M seem coherent with the expected median variation factors for the quantiles X_F, i.e. [1.1; 1.16] for RCP 4.5 and [1.17; 1.25] for RCP 8.5, respectively (see Fig. 8 in Hosseinzadehtalaei et al., 2020), while M belonging to the range [1; 1.6] allows for also reproducing the whole ensemble of change factors for the quantiles X_F, i.e. less than 1 or greater than 1.5 (see Figs. S3-S16 in Hosseinzadehtalaei et al., 2020).

However, these obtained results highlight the independence of $\Delta X_F/X_F$ on the scale parameter θ (which is strictly related to the resolution), thus making impossible the discrimination of higher increases for shorter durations (Hosseinzadehtalaei et al., 2020), unless different values of M factor are assumed (with smaller values for coarser time scales). From Figs. 5-6, $\Delta X_F/X_F$ seems to do not depend in significant way on the shape parameter b, i.e. on the skewness (see Eq. 6). Moreover, application of Eq. (4b) for GEV implies:

$$\lim_{\substack{F\to 0\\(Y_F\to -\infty)}} C(F) = Q = \lim_{\substack{F\to 0\\(Y_F\to -\infty)}} \frac{Y_F \cdot M \cdot \left(1 + \frac{\ln K\Lambda(t_1)}{Y_F}\right)}{Y_F \cdot \left(1 + \frac{\ln \Lambda(t_1)}{Y_F}\right)} = M \tag{12}$$

that restricts the use of GEV with the shape parameter b as invariant in time, only when the plot in Fig. 1 is a horizontal line (i.e. $M = Q$).

Additionally, to directly focus on the rarer events (characterized by the expected larger increases), a user can adopt probability functions which separately consider ordinary and outlier extreme values, like the TCEV (Two-Component Extreme Values, Rossi et al., 1984) distribution, described in Sect. 2.2.

Nevertheless, it should be remarked that this analysis on M and K (and other) factors can be clearly coupled with the adoption of trend functions (linear, non-linear, step, and so on) along the time interval $[t_1; t_2]$ (see Sect. 3).

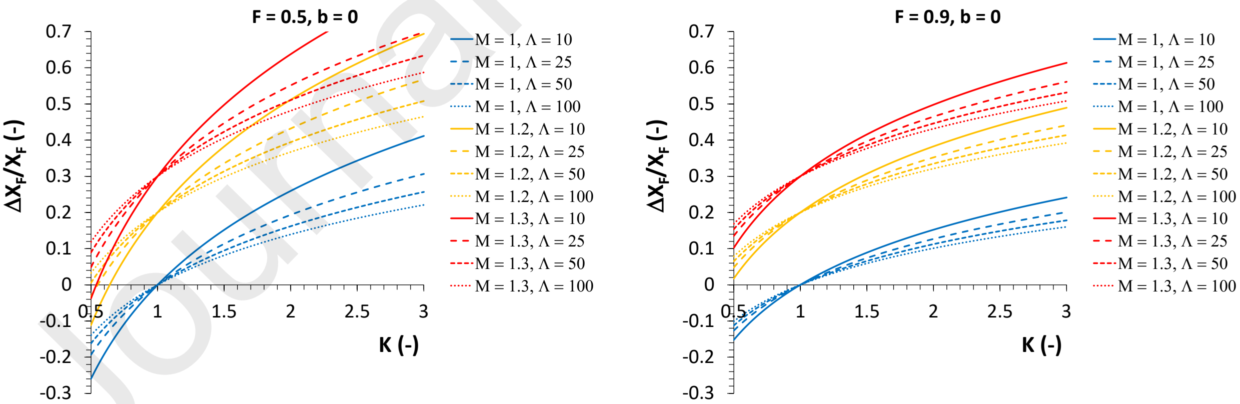

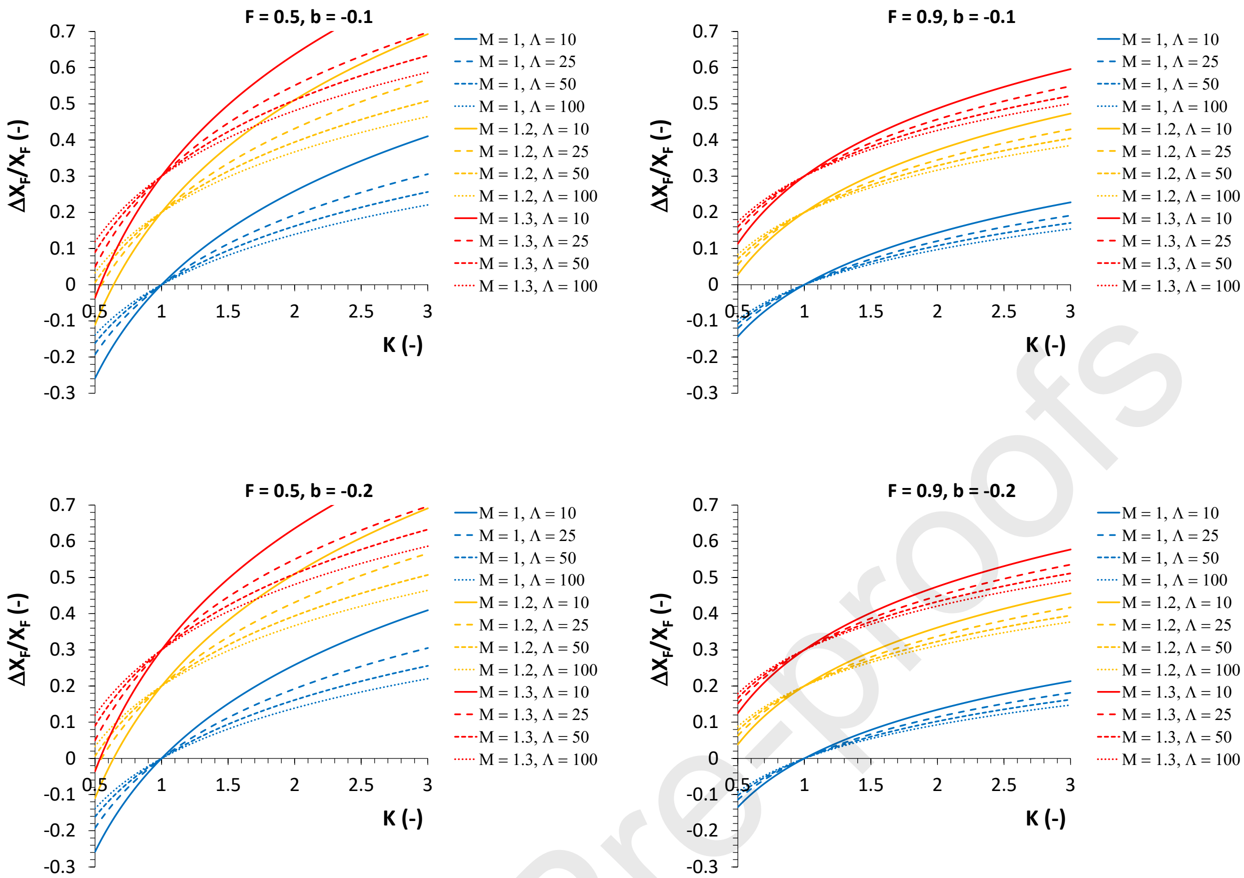

Figure 5. $\Delta X_F/X_F$ for several initial values of Λ and $F = 0.5, 0.9$, when b = 0 (EV1) and $b = -0.1$ and -0.2 (EV2), and by considering $M = 1, 1.2, 1.3$ and K varying from 0.5 to 3.

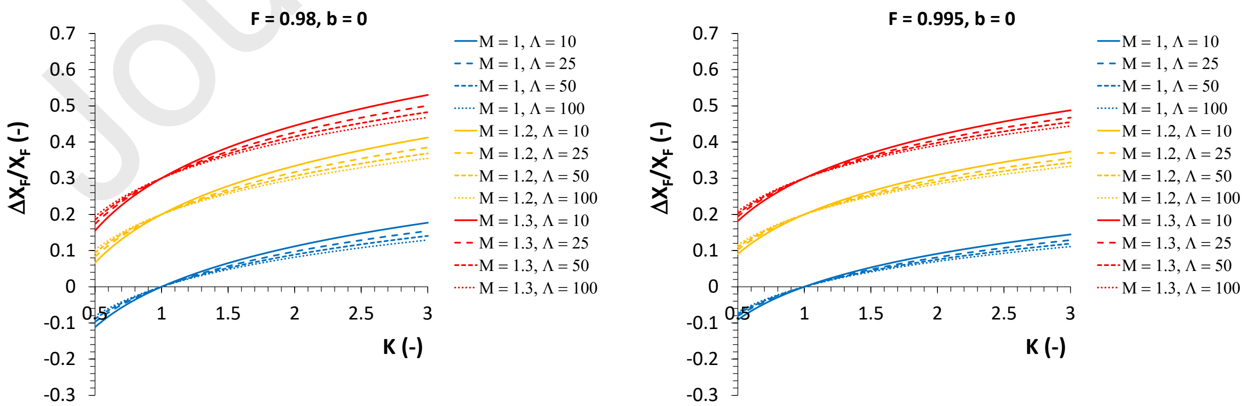

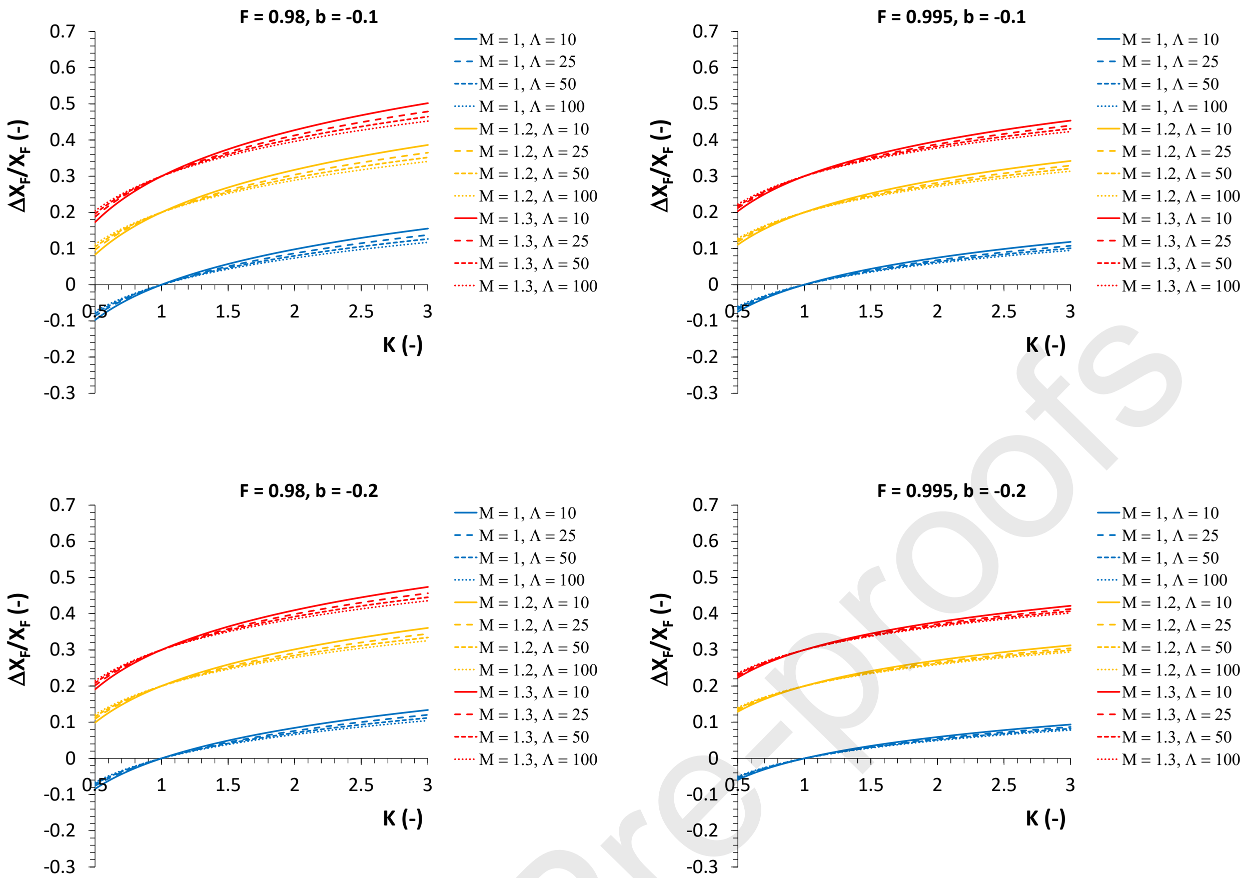

292 **Figure 6**. $\Delta X_F/X_F$ for several initial values of Λ and $F = 0.98, 0.995$, when $b = 0$ (EV1) and $b = -0.1$ and
293 -0.2 (EV2), and by considering $M = 1, 1.2, 1.3$ and K varying from 0.5 to 3.

294

295

2.2. Theoretical background for TCEV distribution

In Sect. 2.1, we focused on Europe and we highlighted that the use of a NS GEV distribution with K factor belong to [0.75; 1] and M inside the range [1; 1.6] allows for reproducing the results in Hosseinzadehtalaei et al. (2020). However, assuming a reduction of the mean annual number of events above a threshold (i.e. $K \leq 1$) seems in contrast with other works (like Papalexiou and Montanari, 2019), in which an increase of frequency for heavy extreme events emerges from data analysis, unless a probability distribution able to discriminate ordinary and “outlier” extreme values is adopted. With this aim, the use of the TCEV (Two Component Extreme Value, Rossi et al., 1984) function appears useful. Its mathematical expression is:

$$F_X(x) = F_X\left(x,\underline{\Phi}\right) = e^{-\Lambda_1 e^{-\frac{x}{\theta_1}} - \Lambda_2 e^{-\frac{x}{\theta_2}}} = e^{-e^{-\left(\frac{x}{\theta_1} - \ln\Lambda_1\right)} - e^{-\left(\frac{x}{\theta_2} - \ln\Lambda_2\right)}} = e^{-e^{-\left(\frac{x}{\theta_1} - \ln\Lambda_1\right)}} \cdot e^{-e^{-\left(\frac{x}{\theta_2} - \ln\Lambda_2\right)}} \quad (13)$$

in which Λ_1 and Λ_2 (with $\Lambda_1 > \Lambda_2$) are the mean annual number for ordinary and outlier events, respectively, while θ_1 and θ_2 (with $\theta_1 < \theta_2$) are the correspondent mean values for intensities, and clearly $\underline{\Phi} = (\Lambda_1, \theta_1, \Lambda_2, \theta_2)$. As shown in the last member of Eq. (13), TCEV can be considered as a product of two EV1 functions. Focusing on Eq. (3), TCEV is obtained from a POT series in which $P_N(n)$ is a Poisson distribution with parameter $\Lambda = \Lambda_1 + \Lambda_2$, while $F_{X,POT}(x)$ is a mixture of two exponential functions:

$$F_{X,POT}(x) = \frac{\Lambda_1}{\Lambda_1 + \Lambda_2} e^{-\frac{x}{\theta_1}} + \frac{\Lambda_2}{\Lambda_1 + \Lambda_2} e^{-\frac{x}{\theta_2}} \quad (14)$$

Starting from these considerations, an overall reduction for $\Lambda = \Lambda_1 + \Lambda_2$ (Sect. 2.1) is clearly coherent with a decrease of Λ_1 (greater) and a simultaneous increase for Λ_2 (smaller). Fig. 7 shows a qualitative example of TCEV curve on an EV1 probabilistic plot, where both ordinary and outlier components are associated to straight lines with equations $Y = \frac{X}{\theta_1} - \ln\Lambda_1$ and $Y = \frac{X}{\theta_2} - \ln\Lambda_2$, respectively.

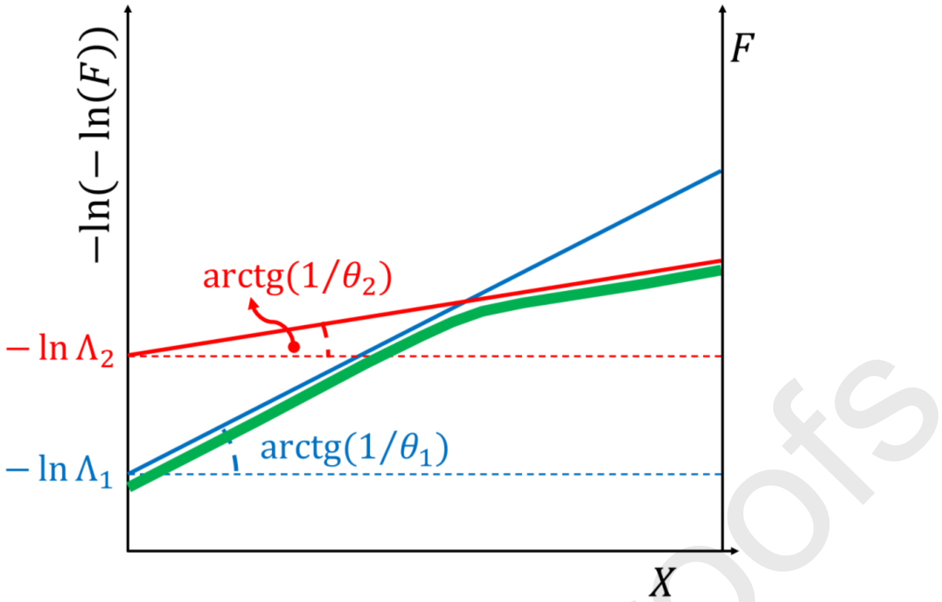

Figure 7. EV1 probabilistic plot. Qualitative example of TCEV (green) curve, and ordinary (straight blue line) and outlier (straight red line) components.

A well-known TCEV formulation, mainly used in contexts of statistical regionalization (Rossi et al., 1984), is obtained by introducing two dimensionless parameters $\theta_* = \frac{\theta_2}{\theta_1}$ and $\Lambda_* = \frac{\Lambda_2}{\Lambda_1^{\frac{1}{\theta_*}}}$:

$$F_X(x) = F_X(x,\underline{\Phi}) = e^{-\Lambda_1 e^{-\frac{x}{\theta_1}} - \Lambda_* \Lambda_1^{\frac{1}{\theta_*}} e^{-\frac{x}{\theta_* \theta_1}}} \tag{15}$$

for which the theoretical skewness only depends on θ_* and Λ_* (Beran et al., 1986), with obviously $\theta_* \geq 1$ and $\Lambda_* \geq 0$, and clearly $\underline{\Phi} = (\Lambda_1, \theta_1, \Lambda_*, \theta_*)$. It should be remarked that Eqs. (13) and (15) coincide with EV1 distribution when $\Lambda_2 = 0$ (i.e. $\Lambda_* = 0$).

Similarly to GEV (Sect. 2.1), we consider the reduced EV1 variable (Rossi et al., 1984), which is defined in this case as:

$$Y = \frac{X}{\theta_1} - \ln\Lambda_1 \tag{16}$$

i.e., by only considering the parameters of the ordinary component. Clearly, also in this case Y is a linear transformation of X, and consequently these two random variables present the same value for skewness and $F_X(x) = F_Y(y)$. Then, it is possible to rewrite Eq. (15) as:

$$F_Y(y) = e^{-e^{-y}-\Lambda_* e^{-\frac{y}{\theta_*}}} = e^{-e^{-y}} \cdot e^{-\Lambda_* e^{-\frac{y}{\theta_*}}} = e^{-e^{-y}} \cdot e^{-e^{-\left(\frac{y}{\theta_*}-ln\Lambda_*\right)}} \tag{17}$$

which allows for a comparison, in terms of probability distribution, among samples with different values of θ_1 and Λ_1 for the ordinary component. Unlike GEV, the TCEV quantile $Y_F = Y_F(\Lambda_*,\theta_*)$ must be estimated by numerical inversion of Eq. (17). However, similarly to GEV with $b \leq 0$, $Y_F(\Lambda_*,\theta_*) \rightarrow +\infty$ and $Y_F(\Lambda_*,\theta_*) \rightarrow -\infty$ when $F_Y(y) \rightarrow 1$ and $F_Y(y) \rightarrow 0$, respectively, and then X_F can computed as:

$$X_F = \theta_1 \cdot (Y_F(\Lambda_*,\theta_*) + \ln\Lambda_1) \tag{18}$$

Concerning a NS approach for TCEV distribution, four plausible scenarios could be considered: a reduction of Λ_1 and a simultaneous increase for Λ_2 (with a total decrease of $\Lambda = \Lambda_1 + \Lambda_2$) is considered for all the considered scenarios. Moreover: Scenario 1 has no change for θ_1 and θ_2, that implies a growth for Λ_*, while θ_* is constant (Fig. 8); Scenario 2 presents an increase for θ_2 and no change for θ_1, and then both Λ_* and θ_* increase (Fig. 9); both θ_1 and θ_2 show the same rate of increment in Scenario 3 (Fig. 10), and consequently Λ_* increases while θ_* is constant (like in Scenario 1, but in this case θ_1 and θ_2 are characterized by a growth); also in Scenario 4, both θ_1 and θ_2 increase, but the rate of increment for θ_2 is greater (Fig. 11), that means an increase for both Λ_* and θ_* (like in Scenario 2, but in this case θ_1 is also growing).

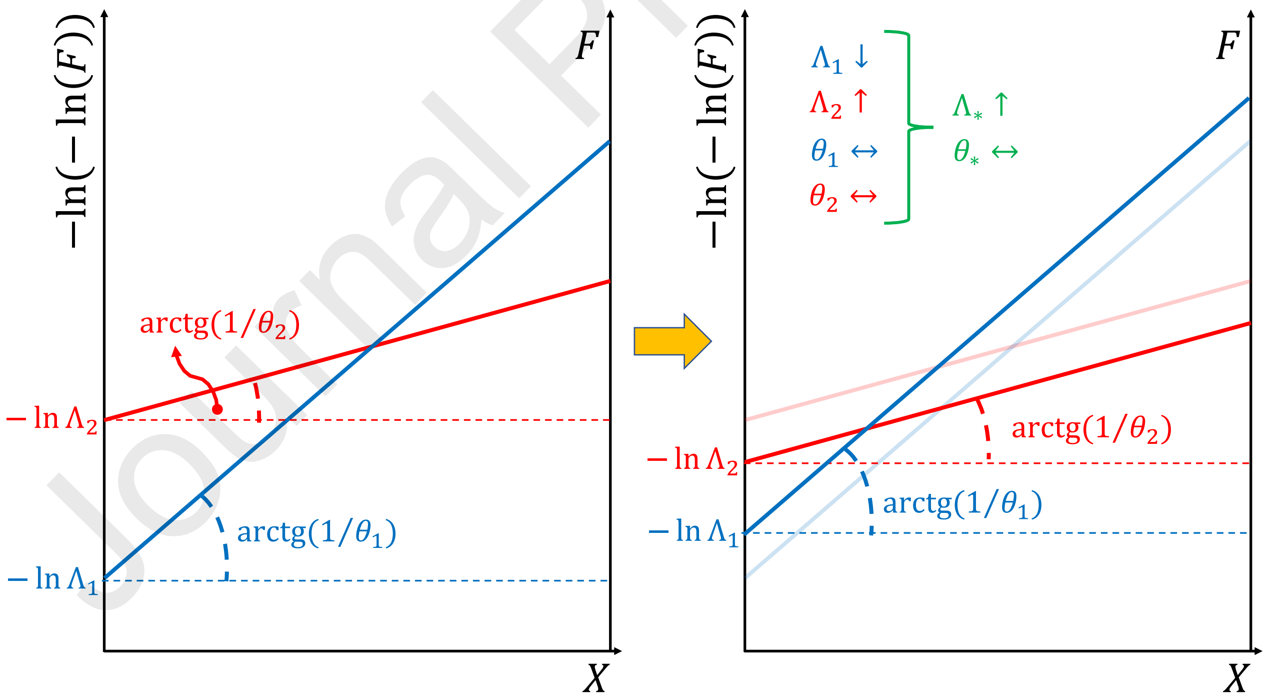

Figure 8. Scenario 1 for NS-TCEV, on EV1 probabilistic plot.

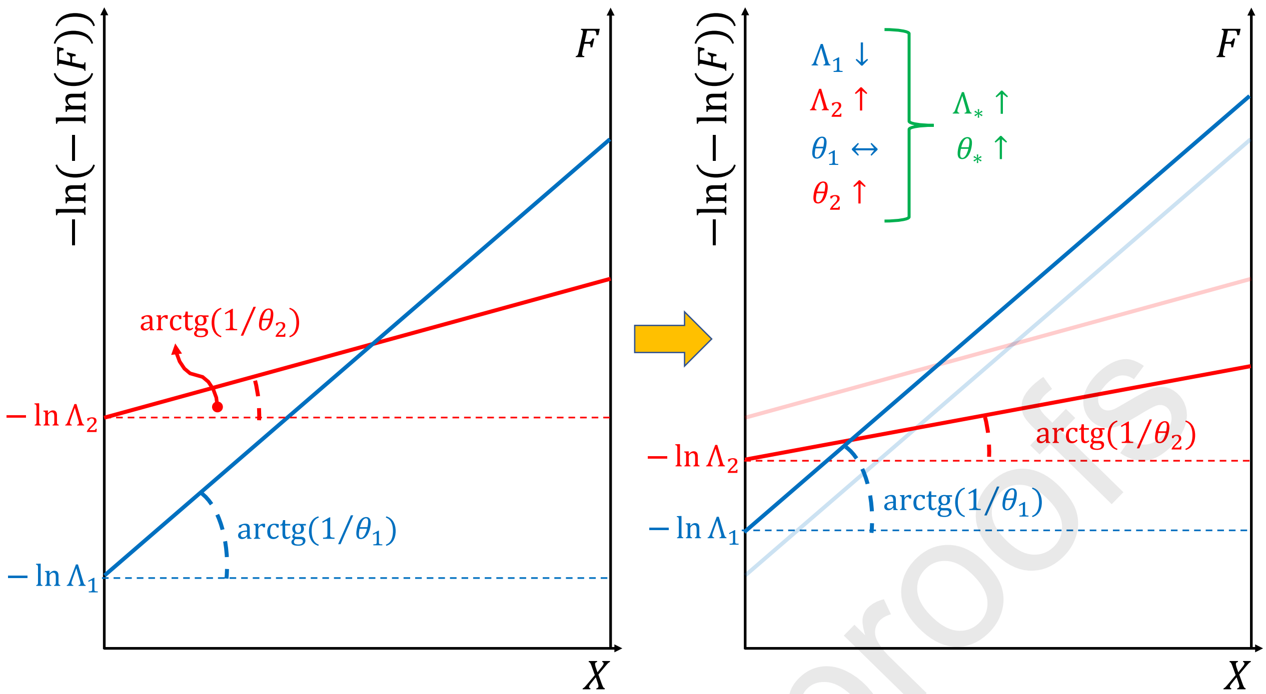

Figure 9. Scenario 2 for NS-TCEV, on EV1 probabilistic plot.

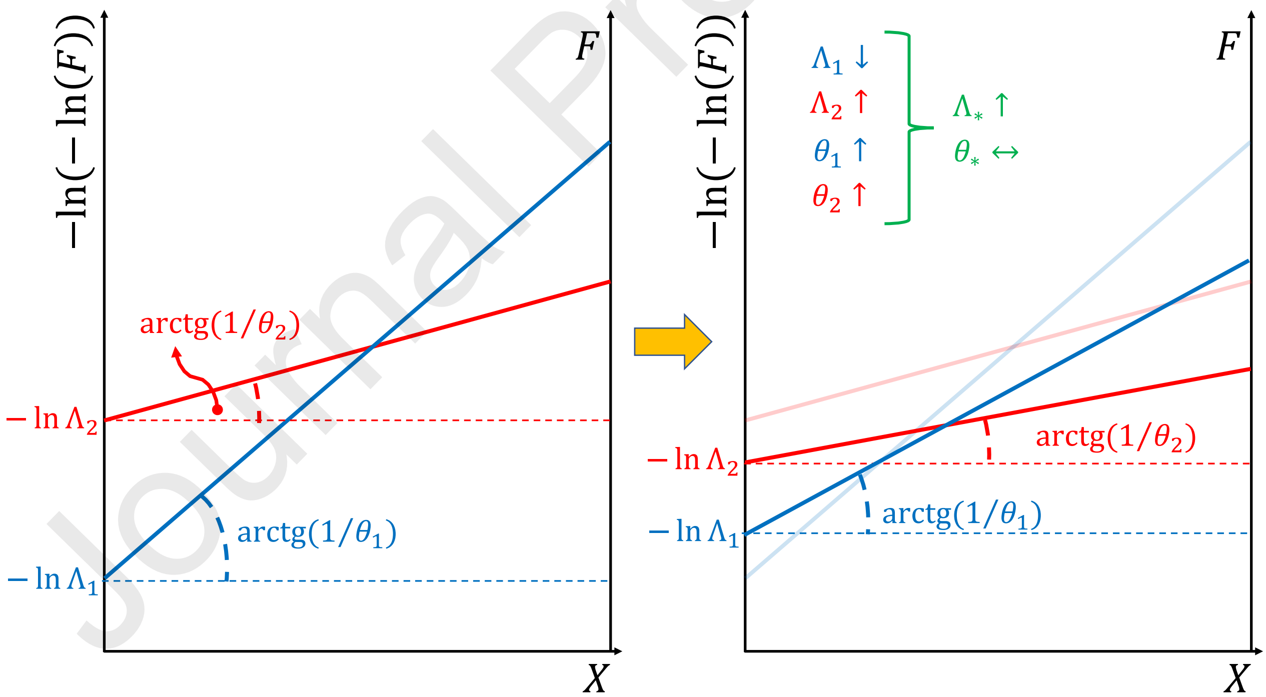

Figure 10. Scenario 3 for NS-TCEV, on EV1 probabilistic plot.

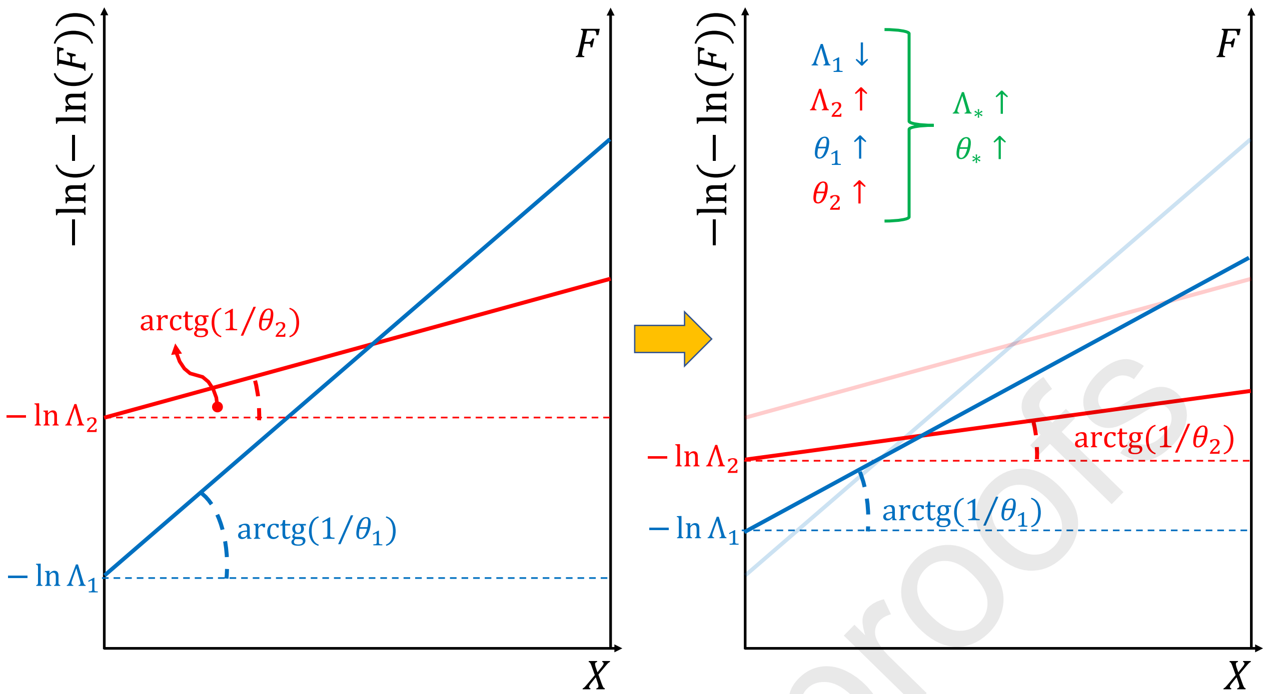

Figure 11. Scenario 4 for NS-TCEV, on EV1 probabilistic plot.

Focusing on $F = 0.98$ and $F = 0.995$ as examples, Figs. 12-13 show the plots of $Y_F(\theta_*,\Lambda_*)$, from which it is possible to quantify the variations of quantile Y_F on the basis on $\Delta\theta_*(t_2-t_1)=\theta_*(t_2)-\theta_*(t_1)$ and $\Delta\Lambda_*(t_2-t_1)=\Lambda_*(t_2)-\Lambda_*(t_1)$. From Figs. 12-13 it is clear that, for $\theta_*(t_1)$ and $\theta_*(t_2)$ very close to 1, the increases of Y_F are not relevant even for a significant growth of Λ_*.

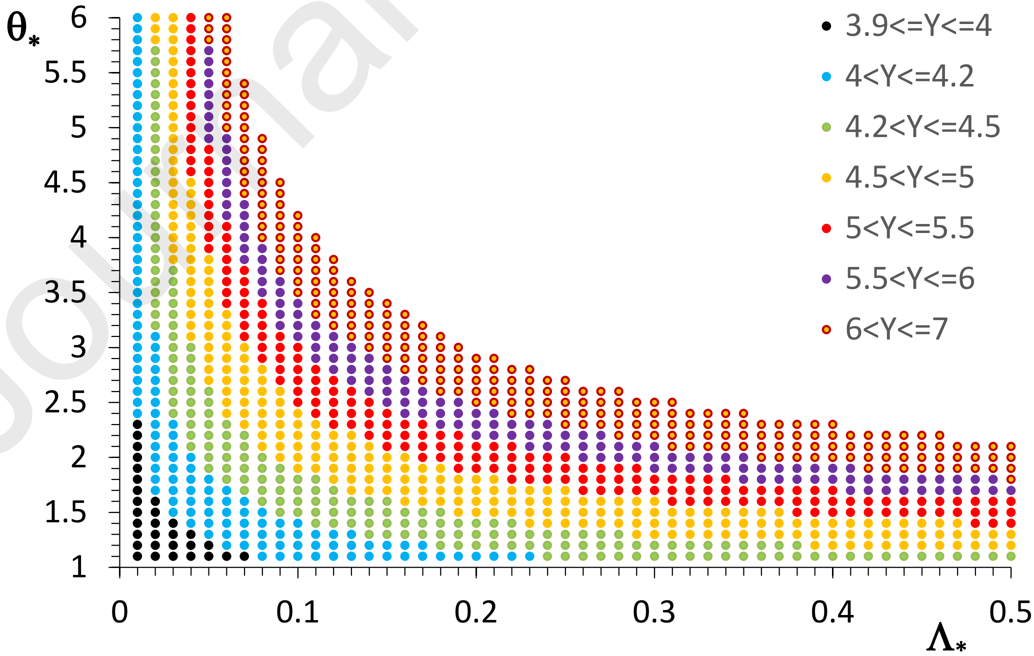

Figure 12. Plot of $Y_{0.98}(\theta_*,\Lambda_*)$, from which it is possible to quantify the variations of quantile Y_F on the basis on $\Delta\theta_*(t_2-t_1)=\theta_*(t_2)-\theta_*(t_1)$ and $\Delta\Lambda_*(t_2-t_1)=\Lambda_*(t_2)-\Lambda_*(t_1)$; it is clear that, for $\theta_*(t_1)$ and $\theta_*(t_2)$ very close to 1, the increases of Y_F are not relevant even for a significant growth of Λ_*.

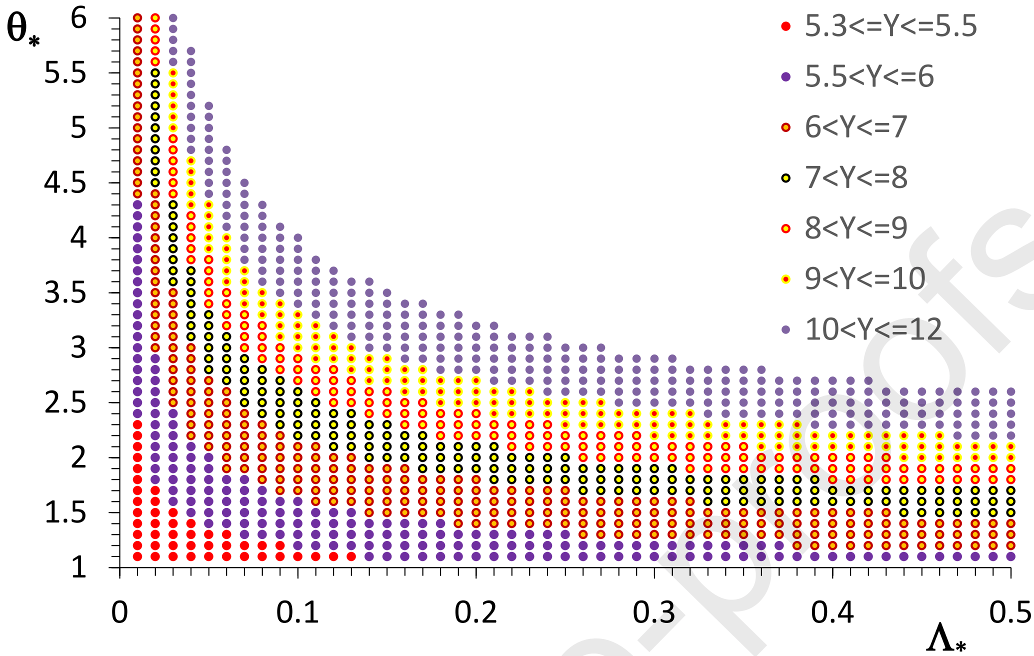

Figure 13. Plot of $Y_{0.995}(\theta_*,\Lambda_*)$, from which it is possible to quantify the variations of quantile Y_F on the basis on $\Delta\theta_*(t_2-t_1)=\theta_*(t_2)-\theta_*(t_1)$ and $\Delta\Lambda_*(t_2-t_1)=\Lambda_*(t_2)-\Lambda_*(t_1)$; it is clear that, for $\theta_*(t_1)$ and $\theta_*(t_2)$ very close to 1, the increases of Y_F are not relevant even for a significant growth of Λ_*.

This behavior is confirmed in Fig. 14, where the dependence of Y_F and the partial derivate $\partial Y_F/\partial\Lambda_*$ on Λ_* are shown for prefixed values of θ_* assumed as constant in time, e.g. Scenarios 1 and 3 represented in Figs. 8 and 10.

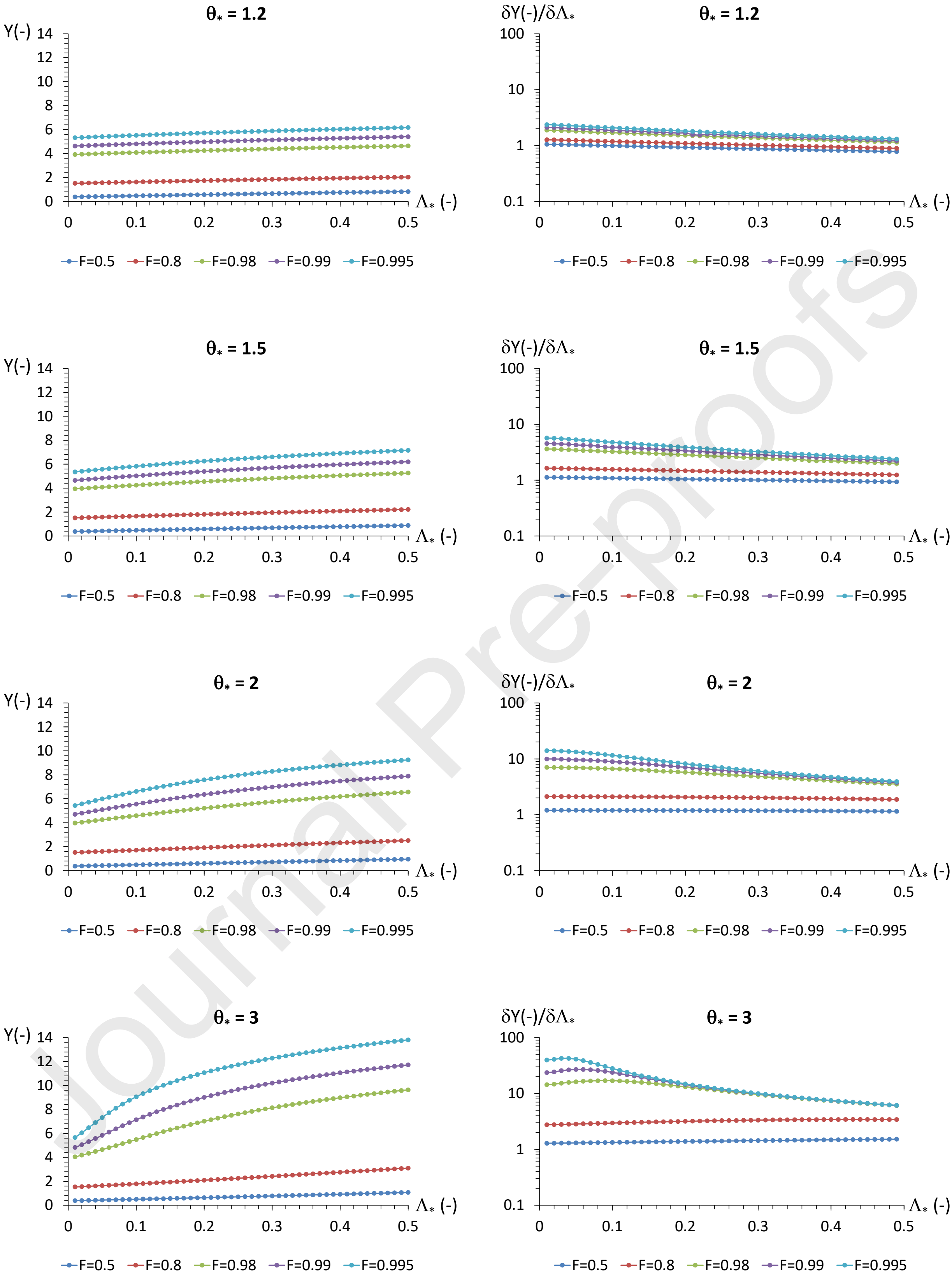
θ* = 1.2
Y(-)
Λ* (-)
δY(-)/δΛ*
θ* = 1.2
Λ* (-)
θ* = 1.5
Y(-)
Λ* (-)
δY(-)/δΛ*
θ* = 1.5
Λ* (-)
θ* = 2
Y(-)
Λ* (-)
δY(-)/δΛ*
θ* = 2
Λ* (-)
θ* = 3
Y(-)
Λ* (-)
δY(-)/δΛ*
θ* = 3
Λ* (-)
F=0.5
F=0.8
F=0.98
F=0.99
F=0.995

Figure 14. Plot of Y_F and $\partial Y_F/\partial \Lambda_*$ depending on Λ_*, for fixed values of θ_*; according to Figs.12-13, θ_* very close to 1 induces (mainly for higher F) smaller variations of Y_F, whatever is the value of Λ_*.

Higher constant values of θ_* induce wider variations of Y_F, mainly for high quantiles, and greater rates of variation (i.e. $\partial Y_F/\partial \Lambda_*$) emerge for small values of Λ_*. Moreover, according to Beran et al. (1986), values of θ_* very close to 1 imply smaller values of skewness, whatever is Λ_*, while higher θ_* induces an increase in skewness. Consequently, if ordinary and outlier extreme events are clearly discriminated like in TCEV distribution, initial skewness seems to represent an important statistical driver for well predicting the effects of potential Climate Change.

To simplify the mathematical approach, it should be noted that TCEV distribution converges to an EV1 distribution for very low F- values (see also the blue line in Fig. 6):

$$\lim_{F\to 0} F_X(x) = \mathrm{e}^{-\mathrm{e}^{-\left(\frac{x}{\theta_1}-\ln\Lambda_1\right)}} \tag{19}$$

and to another EV1 distribution for very high F- values (see also the red line in Fig. 6):

$$\lim_{F\to 1} F_X(x) = \mathrm{e}^{-\mathrm{e}^{-\left(\frac{x}{\theta_2}-\ln\Lambda_2\right)}} \tag{20}$$

Consequently, we can discriminate the tendency of $\Delta X_F/X_F$ when $F\to 0$ and $F\to 1$, similarly to Sect. 2.1:

$$\begin{aligned}\lim_{\substack{F\to 0\\(Y_F\to -\infty)}} \frac{\Delta X_F(t_2-t_1)}{X_F(t_1)} &= \lim_{\substack{F\to 0\\(Y_F\to -\infty)}} C(F)-1 = \lim_{\substack{F\to 0\\(Y_F\to -\infty)}} \frac{Y_F\cdot\theta_1(t_2)\cdot\left(1+\frac{\ln\Lambda_1(t_2)}{Y_F}\right)}{Y_F\cdot\theta_1(t_1)\cdot\left(1+\frac{\ln\Lambda_1(t_1)}{Y_F}\right)}-1\\ &= \lim_{\substack{F\to 0\\(Y_F\to -\infty)}} \frac{Y_F\cdot Q\cdot\theta_1(t_1)\cdot\left(1+\frac{\ln K_1\Lambda_1(t_1)}{Y_F}\right)}{Y_F\cdot\theta_1(t_1)\cdot\left(1+\frac{\ln\Lambda_1(t_1)}{Y_F}\right)}-1 = Q-1\end{aligned} \tag{21a}$$

from which

$$\begin{aligned}\lim_{\substack{F\to 0\\(Y_F\to -\infty)}} C(F) &= \lim_{\substack{F\to 0\\(Y_F\to -\infty)}} \frac{Y_F\cdot\theta_1(t_2)\cdot\left(1+\frac{\ln\Lambda_1(t_2)}{Y_F}\right)}{Y_F\cdot\theta_1(t_1)\cdot\left(1+\frac{\ln\Lambda_1(t_1)}{Y_F}\right)}\\ &= \lim_{\substack{F\to 0\\(Y_F\to -\infty)}} \frac{Y_F\cdot Q\cdot\theta_1(t_1)\cdot\left(1+\frac{\ln K_1\Lambda_1(t_1)}{Y_F}\right)}{Y_F\cdot\theta_1(t_1)\cdot\left(1+\frac{\ln\Lambda_1(t_1)}{Y_F}\right)} = Q\end{aligned} \tag{21b}$$

and

$$\lim_{\substack{F\to 1\\(Y_F\to+\infty)}} \frac{\Delta X_F(t_2-t_1)}{X_F(t_1)} = \lim_{\substack{F\to 1\\(Y_F\to+\infty)}} C(F)-1 = \lim_{\substack{F\to 1\\(Y_F\to+\infty)}} \frac{Y_F\cdot\theta_2(t_2)\cdot\left(1+\frac{\ln\Lambda_2(t_2)}{Y_F}\right)}{Y_F\cdot\theta_2(t_1)\cdot\left(1+\frac{\ln\Lambda_2(t_1)}{Y_F}\right)}-1$$
$$= \lim_{\substack{F\to 1\\(Y_F\to+\infty)}} \frac{Y_F\cdot M\cdot\theta_2(t_1)\cdot\left(1+\frac{\ln K_2\Lambda_2(t_1)}{Y_F}\right)}{Y_F\cdot\theta_2(t_1)\cdot\left(1+\frac{\ln\Lambda_2(t_1)}{Y_F}\right)}-1 = M-1 \qquad (22a)$$

from which:

$$\lim_{\substack{F\to 1\\(Y_F\to+\infty)}} C(F) = \lim_{\substack{F\to 1\\(Y_F\to+\infty)}} \frac{Y_F\cdot\theta_2(t_2)\cdot\left(1+\frac{\ln\Lambda_2(t_2)}{Y_F}\right)}{Y_F\cdot\theta_2(t_1)\cdot\left(1+\frac{\ln\Lambda_1(t_1)}{Y_F}\right)}$$
$$= \lim_{\substack{F\to 1\\(Y_F\to+\infty)}} \frac{Y_F\cdot M\cdot\theta_2(t_1)\cdot\left(1+\frac{\ln K_2\Lambda_2(t_1)}{Y_F}\right)}{Y_F\cdot\theta_2(t_1)\cdot\left(1+\frac{\ln\Lambda_2(t_1)}{Y_F}\right)} = M \qquad (22b)$$

where: $Y_F=\frac{X_F}{\theta_1}-\ln\Lambda_1$ in Eqs. (21a-b) while $Y_F=\frac{X_F}{\theta_2}-\ln\Lambda_2$ in Eqs. (22a-b); $\theta_1(t_2)=Q\cdot\theta_1(t_1)$ and $\Lambda_1(t_2)=K_1\cdot\Lambda_1(t_1)$ in Eqs.(21a-b); $\theta_2(t_2)=M\cdot\theta_2(t_1)$ and $\Lambda_2(t_2)=K_2\cdot\Lambda_2(t_1)$ in Eqs.(22a-b). Like for NS GEV (Sect. 2.1), the use of symbols "M" and "Q" is not ambiguous with respect to Fig. 1: from Eqs. (21a-b) the factor of increase/decrease for θ_1 corresponds to the intercept value of $C(F)$ when $F\to 0$; from Eqs. (22a-b) the factor of increase/decrease for θ_2 corresponds to the asymptotic value of $C(F)$ when $F\to 1$.

Consequently, TCEV distribution is very suitable for application of the proposed methodology; its adoption is clearly not restricted to the case $M=Q$ (see Sect. 2.1). In detail, as also indicated in Fig. 2:

- for any spatial cell and AM duration, starting from a plot $I_F-C(F)$ like in Fig.1 (derived from any climatic model), the increase/decrease factors Q and M (with $M>Q$) for the mean magnitudes θ_1 and θ_2, related to a rain gauge of interest (inside the investigated spatial cell), are clearly input values;
- conversely, the increase/decrease factors K_1 and K_2 for the mean annual frequencies must be calculated, by minimizing the Objective Function S in Eq. (4c), where the values of $C_{F_X}\left(F_i,\underline{\Phi}(t_1),\underline{\Phi}(t_2)\right)$ depend on the input quantities $\Lambda_1(t_1)$, $\theta_1(t_1)$, $\Lambda_2(t_1)$, $\theta_2(t_1)$, Q, M, and on K_1, K_2 (to be estimated);
- as widely discussed in the next Sect. 3, the possibility of also evaluating K_1 and K_2, with respect to the sole information of Q and M (deducible from the mere use of Fig. 1), allows to investigate if some statistical "drivers" play a crucial role for the (significant or not) increase/reduction of frequencies of extreme events (in Sect. 3.2, the importance of the skewness at time t_1 will be highlighted). In other words, starting from a fixed plot like in Fig.1, we analyze if different values of the identified driver(s) can induce different combinations K_1, K_2, and consequently distinct hazard evaluations for the horizon $[t_1; t_2]$ (Sect. 3.3).

As regard the last bullet point, two simple kinds of temporal evolution for the function $\Lambda_1(t)$, $\theta_1(t)$, $\Lambda_2(t)$ and $\theta_2(t)$ are assumed in this work:

- from the former (Fig. 15), indicated as E1, all the TCEV parameters are linear functions in the interval $[t_1; t_2]$, without any change of slope (i.e., with a constant value of the derivative). According to the previous considerations, it is expected that $\Lambda_1(t)$ is a decreasing function, while $\Lambda_2(t)$, $\theta_1(t)$ and $\theta_2(t)$ are increasing functions with $M > Q$ (and then only the fourth scenario, previously represented in Fig. 11, can be plausible for evaluation of CC effects in this context). The results obtained in Sect. 3.1 will confirm these expected behaviors;
- on the basis on the latter considered kind of temporal evolution (Fig. 16), named as E2, all the TCEV parameters are linear increasing ($\Lambda_2(t)$, $\theta_1(t)$, $\theta_2(t)$, with $M > Q$), or decreasing ($\Lambda_1(t)$) functions until t_* , with $t_1 < t_* < t_2$, and then constant along the interval $[t_*;t_2]$. This pattern is suitable for "stabilization scenarios", in which the rate of radiative forcing is stopped when prefixed thresholds for emissions of greenhouse gasses are reached (Nazarenko et al., 2015).

Once assumed the kind of temporal evolution for the TCEV parameters, it is possible to evaluate for any design value x of interest:

- the Hazard $H(x,t_1,t_2)$ (Salas and Obeysekera, 2014; Volpi, 2019):

$$H(x,t_1,t_2) = 1 - \prod_{j=t_1}^{t_2} F_X(x,\Lambda_1(j),\Lambda_2(j),\theta_1(j),\theta_2(j)) \tag{23}$$

  which corresponds to the probability that the event $X > x$ occurs at least one time into a period of interest, in this case the interval $[t_1; t_2]$;
- the stationary case for the Hazard:

$$H_{Stat}(x,t_1,t_2) = 1 - [F_X(x,\Lambda_1(t_1),\Lambda_2(t_1),\theta_1(t_1),\theta_2(t_1))]^{(t_2-t_1)} \tag{24}$$

  where all the TCEV parameters are invariant along the interval $[t_1; t_2]$, with respect to the values assumed at t_1;
- the Hazard variation:

$$\Delta H(x,t_1,t_2) = H(x,t_1,t_2) - H_{Stat}(x,t_1,t_2) \tag{25}$$

  that clearly quantifies CC effects in terms of hazard.

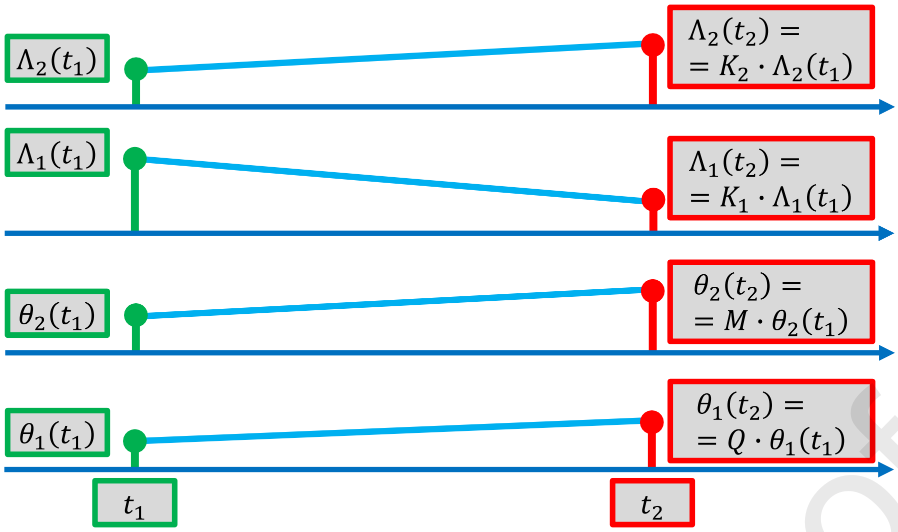

Figure 15. E1 temporal evolution for the function $\Lambda_1(t)$, $\theta_1(t)$, $\Lambda_2(t)$ and $\theta_2(t)$

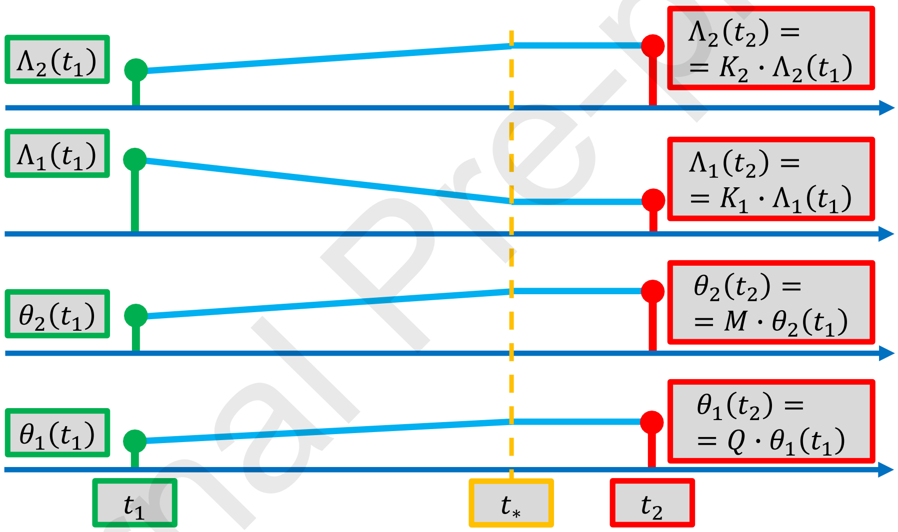

Figure 16. E2 temporal evolution for the function $\Lambda_1(t)$, $\theta_1(t)$, $\Lambda_2(t)$ and $\theta_2(t)$

3. Numerical experiments and discussion

As reported in Sect. 2, the elaborations discussed here are related to the TCEV distribution only, particularly suitable to discriminate outliers from ordinary extreme events. The dataset is introduced In Sect. 3.1, while the numerical experiments are presented in Sects. 3.2 and 3.3.

3.1. Dataset

In Italy, hydrological monitoring has been performed by National Hydrographic and Mareographic Service (SIMN) for several years. In 2002, the entire monitoring network was transferred to regions with a Prime Ministerial Decree of the 24/07/2002. Therefore, data management was assigned in most of the cases to the Regional Department of Civil Protection (or to Regional Agencies). A list of the hydrological agencies that conduct the data collection and management after the dismantlement of SIMN are reported in Mazzoglio et al. (2020). Information about the data policies and how raw data can be accessed is also included. Hydrological data can be also accessed through the hydrological yearbooks (freely available at http://www.bio.isprambiente.it/annalipdf/). Data at daily resolution are provided by The Italian National Institute for Environmental Protection and Research (ISPRA) in the form of a unified and open-access system, called National System for the Collection, Elaboration and Diffusion of Climatological Data (SCIA; Desiato et al., 2007).

Several studies concerning TCEV application for extreme rainfall series (at daily and sub-daily resolutions) were carried out in Italy (see, for example, Versace et al., 1989; Ferro and Porto, 1999; Boni et al., 2006; Caporali et al., 2008; De Luca and Galasso, 2018; Forestieri et al., 2018b). Recently, De Luca and Napolitano (2023) demonstrated that the major part of sample values of skewness for updated daily AM series can be modelled with Λ_* comprised between 0 (i.e. by using an EV1 distribution) and 0.10-0.15, with θ_* at most equal to 2.5-3. For sub-daily time series (usually more skewed), when their sample size is significantly smaller than daily one, it is frequent to assume the same values of daily Λ_* and θ_* and then to carry out estimation only for Λ_1 and θ_1, to respect the parametric parsimony.

Building upon the insights gathered from previous works, we selected six plausible groups of TCEV parameters (which provide values of quantiles that are coherent with time series in Italy), for the durations $d = 1$, 3, 6, 12 and 24 h and related to $t = t_1$ (i.e. before the beginning of any possible climate change scenario), which can be schematized in two main levels:

1. the finer resolutions have a larger ratio $\frac{\Lambda_2(t_1)}{\Lambda_1(t_1)}$ with respect to the coarser durations, that means greater mean annual frequencies $\Lambda_2(t_1)$ for outliers and smaller values for $\Lambda_1(t_1)$ when $d = 1$, 3 h;
2. all the durations are characterized by the same ratio $\frac{\Lambda_2(t_1)}{\Lambda_1(t_1)}$;

each one with three sub levels:

a. the finer resolutions present greater values of $\theta_*(t_1)$ with respect to the coarser ones (characterized by $\theta_*(t_1)$ closer to 1), that means time series are more skewed when $d = 1$, 3, 6 h, while an "EV1 alike" skewness is related to $d = 12$, 24 h;
b. all the durations are characterized by $\theta_*(t_1) = 2$, i.e. all the time series are more significantly skewed with respect to EV1;
c. all the durations are characterized by $\theta_*(t_1) = 1.2$, i.e. all the time series present a skewness not so far from $\gamma_1 = 1.14$.

The last two sub levels are coherent with the hypothesis of assuming the same daily set (Λ_*, θ_*) for $d = 1$, 3, 6, 12 and 24 h, when sample size of sub daily time series is considerably smaller than the daily one. Overall, these six groups are indicated in the following as G_{1a}, G_{1b}, G_{1c}, G_{2a}, G_{2b} and G_{2c} (see Tables 1-6, in which the quantiles $X_{0.9}(t_1)$, $X_{0.99}(t_1)$ and $X_{0.995}(t_1)$ are also indicated).

As regards the evaluation of CC effects, according to Hosseinzadehtalaei et al. (2020), we chose a temporal horizon $t_2 - t_1$=100 years and we considered, for M and Q, the median values of RCP4.5, derived for the entire Europe (see Table 7), which can be assumed as valid for Italy (see Figs. 8 and S3 in Hosseinzadehtalaei et al., 2020). Based on all these assumptions and on Sect. 2.2: Sect. 3.1 refers to the estimation of $\theta_1(t_2)$, $\theta_2(t_2)$, $\Lambda_1(t_2)$ and $\Lambda_2(t_2)$ for the six groups of plausible TCEV parameters for Italy; examples of hazard evaluation are discussed in Sect. 3.2, in which the temporal evolutions E1 and E2 (Figs. 15-16) for $\theta_1(t)$, $\theta_2(t)$, $\Lambda_1(t)$, $\Lambda_2(t)$, with $t \in [t_1, t_2]$, are assumed. Moreover, from $\theta_2(t_2) = M \cdot \theta_2(t_1)$ and $\theta_1(t_2) = Q \cdot \theta_1(t_1)$, it can be highlighted that:

$$\theta_*(t_2) = \frac{\theta_2(t_2)}{\theta_1(t_2)} = \frac{M \cdot \theta_2(t_1)}{Q \cdot \theta_1(t_1)} = \frac{M}{Q} \cdot \theta_*(t_1) \tag{26}$$

and then the ratio M/Q represents the variation factor for θ_* parameters. For RCP4.5 scenario, there is an increase for all the durations, between about 6% and 7% (see the third column of Table 7).

Table 1. G_{1a} group: TCEV parameters and values of quantiles $X_{0.9}(t_1)$, $X_{0.99}(t_1)$ and $X_{0.995}(t_1)$

d (h)	$\Lambda_1(t_1)$ (-)	$\theta_1(t_1)$ (mm)	$\Lambda_*(t_1)$ (-)	$\theta_*(t_1)$ (-)	$\Lambda_2(t_1)$ (-)	$\theta_2(t_1)$ (mm)	$X_{0.9}(t_1)$ (mm)	$X_{0.99}(t_1)$ (mm)	$X_{0.995}(t_1)$ (mm)
1	15	8	0.169	2.5	0.5	20	45	80	93
3	20	12	0.101	2	0.45	24	67	103	115
6	25	15	0.080	2	0.4	30	86	129	144
12	30	22	0.036	1.5	0.35	33	126	180	196
24	30	30	0.018	1.2	0.3	36	170	241	262

Table 2. G_{1b} group: TCEV parameters and values of quantiles $X_{0.9}(t_1)$, $X_{0.99}(t_1)$ and $X_{0.995}(t_1)$

d (h)	$\Lambda_1(t_1)$ (-)	$\theta_1(t_1)$ (mm)	$\Lambda_*(t_1)$ (-)	$\theta_*(t_1)$ (-)	$\Lambda_2(t_1)$ (-)	$\theta_2(t_1)$ (mm)	$X_{0.9}(t_1)$ (mm)	$X_{0.99}(t_1)$ (mm)	$X_{0.995}(t_1)$ (mm)

1	15	8	0.129	2	0.5	16	43	68	77
3	20	12	0.101	2	0.45	24	67	103	115
6	25	15	0.080	2	0.4	30	86	129	144
12	30	22	0.064	2	0.35	44	129	190	211
24	30	30	0.055	2	0.3	60	175	256	284

Table 3. G_{1c} group: TCEV parameters and values of quantiles $X_{0.9}(t_1)$, $X_{0.99}(t_1)$ and $X_{0.995}(t_1)$

d (h)	$\Lambda_1(t_1)$ (-)	$\theta_1(t_1)$ (mm)	$\Lambda_*(t_1)$ (-)	$\theta_*(t_1)$ (-)	$\Lambda_2(t_1)$ (-)	$\theta_2(t_1)$ (mm)	$X_{0.9}(t_1)$ (mm)	$X_{0.99}(t_1)$ (mm)	$X_{0.995}(t_1)$ (mm)
1	15	8	0.052	1.2	0.5	9.6	40	59	65
3	20	12	0.037	1.2	0.45	14.4	64	92	101
6	25	15	0.027	1.2	0.4	18	83	118	129
12	30	22	0.021	1.2	0.35	26.4	125	177	192
24	30	30	0.018	1.2	0.3	36	170	241	262

Table 4. G_{2a} group: TCEV parameters and values of quantiles $X_{0.9}(t_1)$, $X_{0.99}(t_1)$ and $X_{0.995}(t_1)$

d (h)	$\Lambda_1(t_1)$ (-)	$\theta_1(t_1)$ (mm)	$\Lambda_*(t_1)$ (-)	$\theta_*(t_1)$ (-)	$\Lambda_2(t_1)$ (-)	$\theta_2(t_1)$ (mm)	$X_{0.9}(t_1)$ (mm)	$X_{0.99}(t_1)$ (mm)	$X_{0.995}(t_1)$ (mm)
1	20	8	0.151	2.5	0.5	20	47	80	93

3	20	12	0.112	2	0.5	24	67	104	117
6	20	15	0.112	2	0.5	30	84	130	146
12	20	22	0.068	1.5	0.5	33	119	174	191
24	20	30	0.041	1.2	0.5	36	159	231	252

Table 5. G_{2b} group: TCEV parameters and values of quantiles $X_{0.9}(t_1)$, $X_{0.99}(t_1)$ and $X_{0.995}(t_1)$

d (h)	$\Lambda_1(t_1)$ (-)	$\theta_1(t_1)$ (mm)	$\Lambda_*(t_1)$ (-)	$\theta_*(t_1)$ (-)	$\Lambda_2(t_1)$ (-)	$\theta_2(t_1)$ (mm)	$X_{0.9}(t_1)$ (mm)	$X_{0.99}(t_1)$ (mm)	$X_{0.995}(t_1)$ (mm)
1	20	8	0.112	2	0.5	16	45	69	78
3	20	12	0.112	2	0.5	24	67	104	117
6	20	15	0.112	2	0.5	30	84	130	146
12	20	22	0.112	2	0.5	44	123	191	214
24	20	30	0.112	2	0.5	60	168	260	292

Table 6. G_{2c} group: TCEV parameters and values of quantiles $X_{0.9}(t_1)$, $X_{0.99}(t_1)$ and $X_{0.995}(t_1)$

d (h)	$\Lambda_1(t_1)$ (-)	$\theta_1(t_1)$ (mm)	$\Lambda_*(t_1)$ (-)	$\theta_*(t_1)$ (-)	$\Lambda_2(t_1)$ (-)	$\theta_2(t_1)$ (mm)	$X_{0.9}(t_1)$ (mm)	$X_{0.99}(t_1)$ (mm)	$X_{0.995}(t_1)$ (mm)
1	20	8	0.041	1.2	0.5	9.6	42	62	67
3	20	12	0.041	1.2	0.5	14.4	64	92	101

6	20	15	0.041	1.2	0.5	18	80	115	126
12	20	22	0.041	1.2	0.5	26.4	117	169	185
24	20	30	0.041	1.2	0.5	36	159	231	252

Table 7. Assumed Q and M values, referred to RCP4.5.

$\boldsymbol{d}$ (h)	$\boldsymbol{Q}$ (-)	$\boldsymbol{M}$ (-)	$\boldsymbol{M/Q}$ (-)
1	1.106	1.186	1.072
3	1.106	1.186	1.072
6	1.101	1.176	1.068
12	1.095	1.167	1.066
24	1.089	1.155	1.061

3.2. Estimation of $\boldsymbol{\theta_1(t_2)}$, $\boldsymbol{\theta_2(t_2)}$, $\boldsymbol{\Lambda_1(t_2)}$ and $\boldsymbol{\Lambda_2(t_2)}$

Starting from the "known" values of M and Q, the minimization of Eq. (4c) in terms of K_1 and K_2 for all the durations were carried out by considering the following $n_F = 6$ frequencies F_i: 0.5, 0.8, 0.9, 0.95, 0.98 and 0.99. Powell's algorithm (Press et al., 1988) was adopted, and the search of the minimum was made from the initial point (1, 1) for (K_1, K_2), i.e. from the situation at t_1. The obtained results are shown in Figs. 17-18 and in Tables 8-9, where K_{TOT} is defined as:

$$K_{TOT} = \frac{K_1 \cdot \Lambda_1(t_1) + K_2 \cdot \Lambda_2(t_1)}{\Lambda_1(t_1) + \Lambda_2(t_1)} \tag{27}$$

and it represents the increase/decrease factor for the overall frequency $\Lambda(t_1) = \Lambda_1(t_1) + \Lambda_2(t_1)$, e.g. $\Lambda(t_2) = K_{TOT} \cdot \Lambda(t_1)$. As expected in Sects. 2.1 and 2.2, K_{TOT} is always less than 1, but the reduction for $\Lambda_1(.)$ and the increase for $\Lambda_2(.)$ are strongly marked when $\Lambda_*(t_1)\rightarrow 0$ and $\theta_*(t_1)\rightarrow 1$, that means a time series with an "EV1 alike" skewness at t_1.

These outcomes can be justified by the analysis of the previous Figs. 12-13 (Sect. 2.2): if $\theta_*(t_1) = 1.2$ and $M/Q \in [1.061;1.072]$ (see Table 7), then $\theta_*(t_2) \in [1.27;1.29]$ and consequently, as both $\theta_*(t_1)$ and $\theta_*(t_2)$ are close to 1, a unit increment for Y_F requires a significant growth of Λ_*, that can be reached with (both or at least one condition) $K_2 \gg 1$ (i.e. $\Lambda_2(t_2) \gg \Lambda_2(t_1)$) and $K_1 \ll 1$ (i.e. $\Lambda_1(t_2) \ll \Lambda_1(t_1)$). Figs. 19-24 show the vectors of variation on the plot (Λ_*, θ_*) for each investigated group of TCEV parameters. This analysis clearly highlights the crucial role played by the skewness at t_1, and in particular by $\theta_*(t_1)$: in order to respect prefixed change factors (from assumed climatic projections), if $\theta_*(t_1)$ is close to 1 and $\theta_*(t_2) = \frac{M}{Q} \cdot \theta_*(t_1)$ is consequently not so far from $\theta_*(t_1)$ (i.e., less than 1.8-2, as the ratio M/Q should rarely assume values greater than 1.5 in all the RCP outputs, see also Hosseinzadehtalaei et al., 2020), then substantial variations in frequencies (e.g. $\Lambda_*(.)$) are necessary (see Figs. 12-13 and 19-24). Moreover, these results are coherent with Papalexiou and Montanari (2019), in which an increase of frequency for heavy extreme events emerges for daily time series, usually less skewed than the hourly scales.

Table 8. Estimation of K_1, K_2 and K_{TOT} for the TCEV parametric groups G_{1a}, G_{1b}, G_{1c}

	G_{1a}			**G_{1b}**			**G_{1c}**		
d (h)	K_1 (-)	K_2 (-)	K_{TOT} (-)	K_1 (-)	K_2 (-)	K_{TOT} (-)	K_1 (-)	K_2 (-)	K_{TOT} (-)
1	0.96	1.01	0.96	0.95	1.18	0.96	0.70	5.46	0.85
3	0.95	1.27	0.96	0.95	1.27	0.96	0.68	7.64	0.83
6	0.94	1.35	0.94	0.94	1.35	0.94	0.70	9.35	0.84
12	0.88	3.37	0.91	0.95	1.46	0.95	0.71	12.01	0.84
24	0.72	13.56	0.85	0.95	1.55	0.95	0.72	13.56	0.85

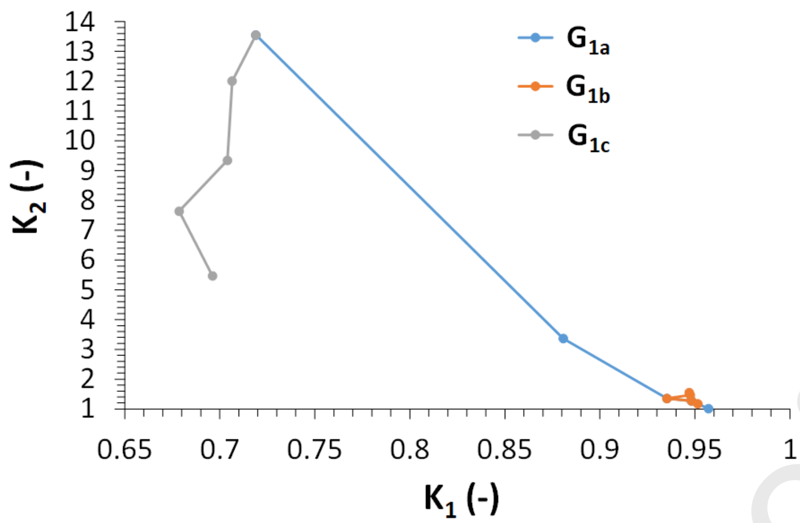

547

548 **Figure 17.** Estimation of K_1, K_2 for the TCEV parametric groups G_{1a}, G_{1b}, G_{1c}

549

550 **Table 9.** Estimation of K_1, K_2 and K_{TOT} for the TCEV parametric groups G_{2a}, G_{2b}, G_{2c}

	G_{2a}			G_{2b}			G_{2c}		
d (h)	K_1 (-)	K_2 (-)	K_{TOT} (-)	K_1 (-)	K_2 (-)	K_{TOT} (-)	K_1 (-)	K_2 (-)	K_{TOT} (-)
1	0.98	1.03	0.98	0.94	1.24	0.95	0.67	7.10	0.83
3	0.96	1.21	0.96	0.96	1.21	0.96	0.67	7.10	0.83
6	0.93	1.21	0.93	0.93	1.21	0.93	0.70	6.47	0.85
12	0.86	2.20	0.89	0.95	1.18	0.95	0.72	6.21	0.85
24	0.73	6.12	0.86	0.95	1.18	0.95	0.73	6.12	0.86

551

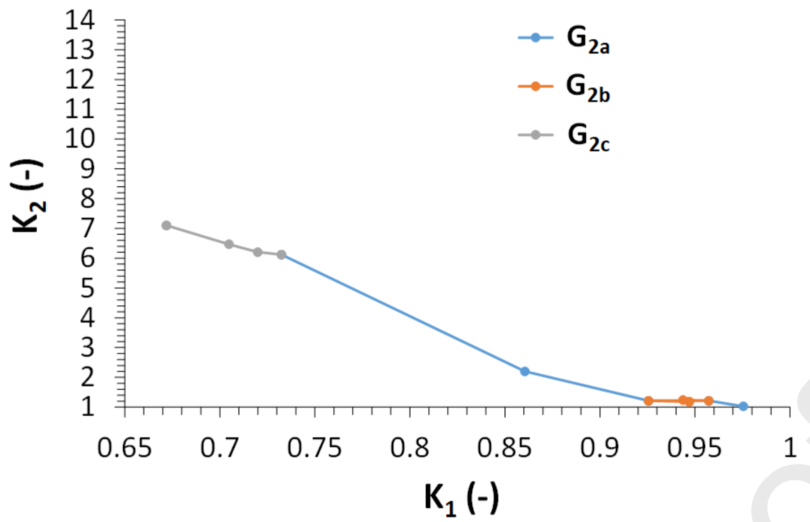

552

553 **Figure 18.** Estimation of K_1, K_2 for the TCEV parametric groups G_{2a}, G_{2b}, G_{2c}

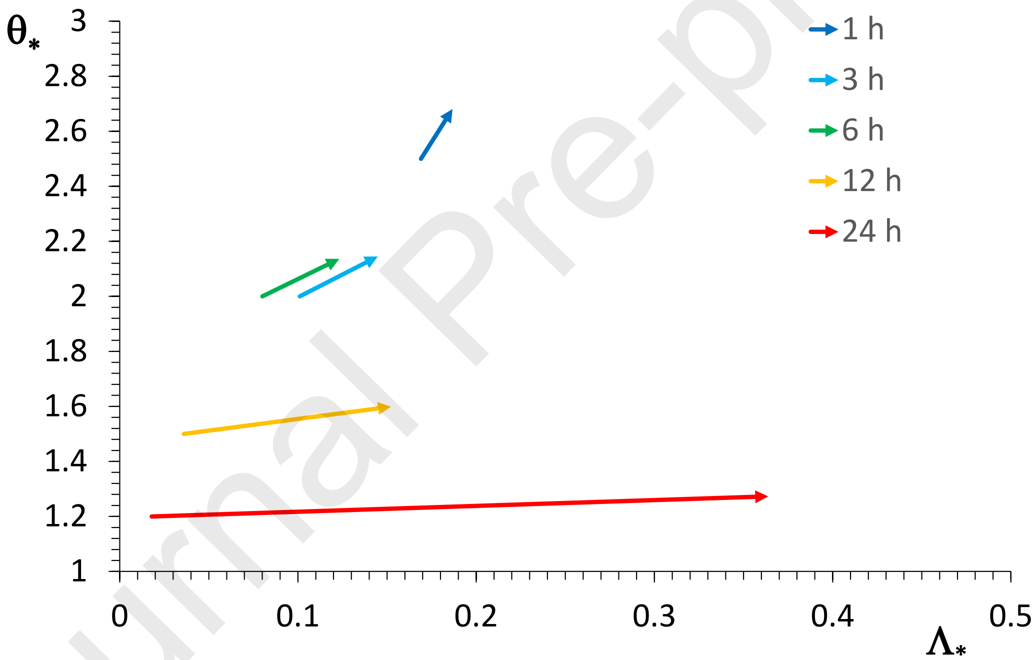

554

555 **Figure 19.** Vectors of variation on the plot (Λ_*, θ_*) for the TCEV parametric groups G_{1a}

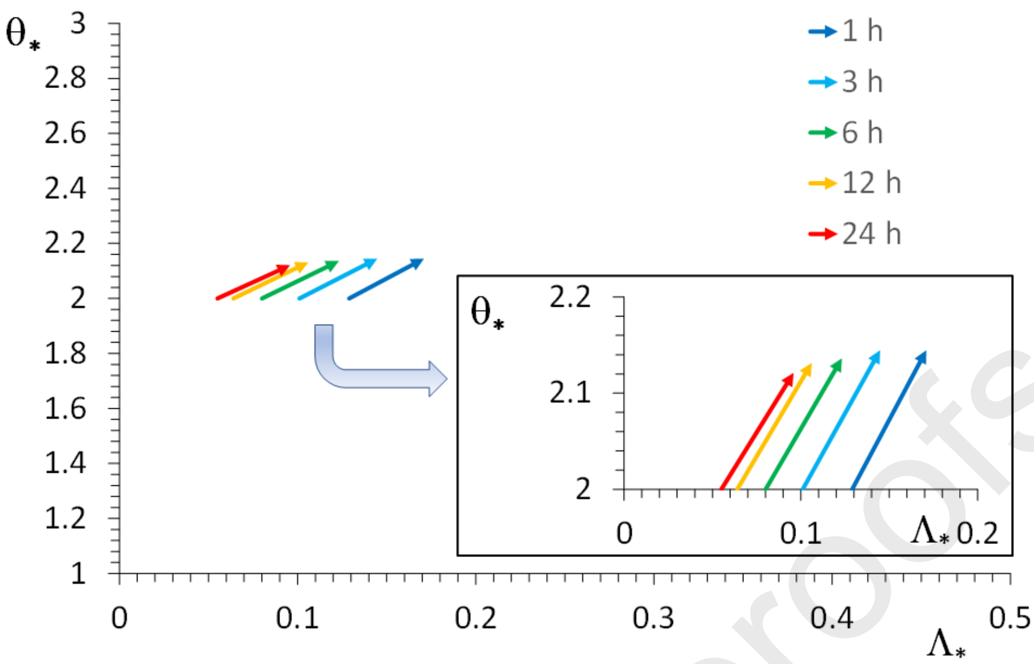

Figure 20. Vectors of variation on the plot (Λ_*, θ_*) for the TCEV parametric groups G_{1b}

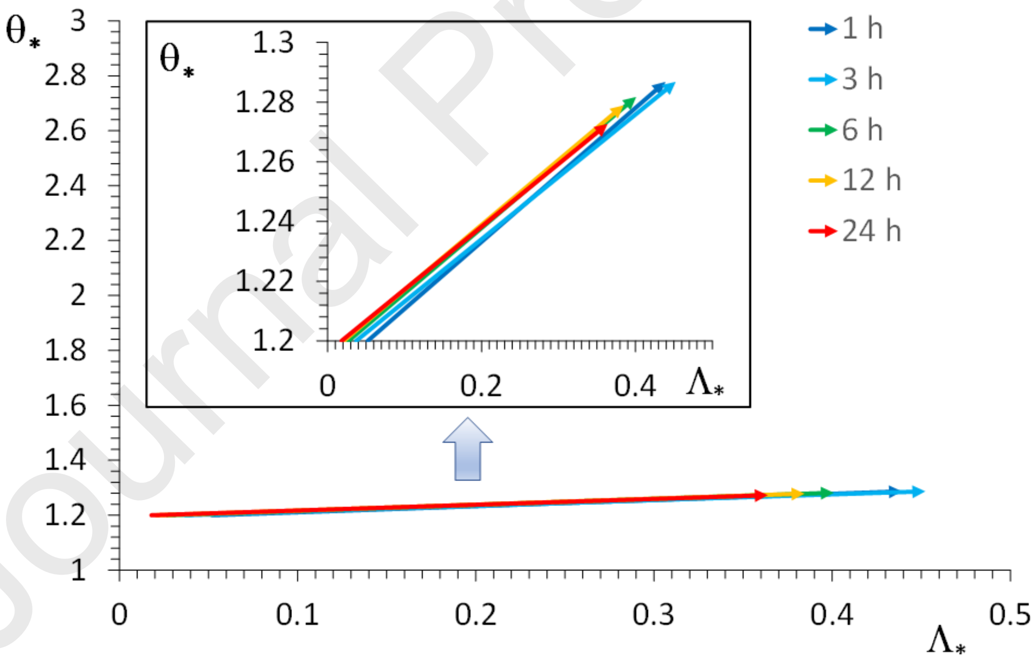

Figure 21. Vectors of variation on the plot (Λ_*, θ_*) for the TCEV parametric groups G_{1c}

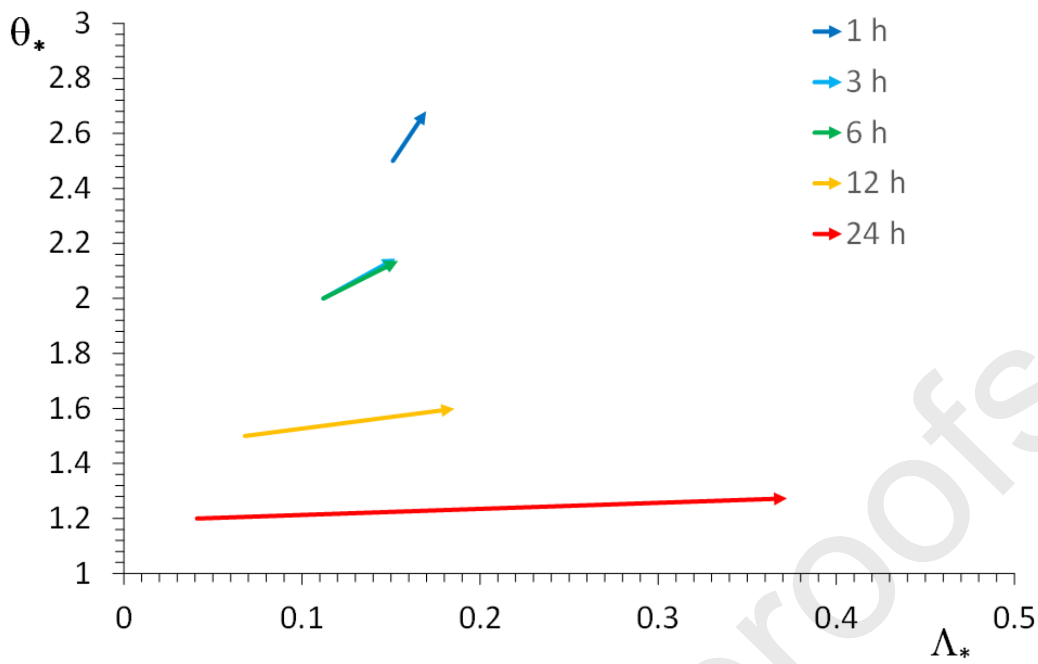

Figure 22. Vectors of variation on the plot (Λ_*, θ_*) for the TCEV parametric groups G_{2a}

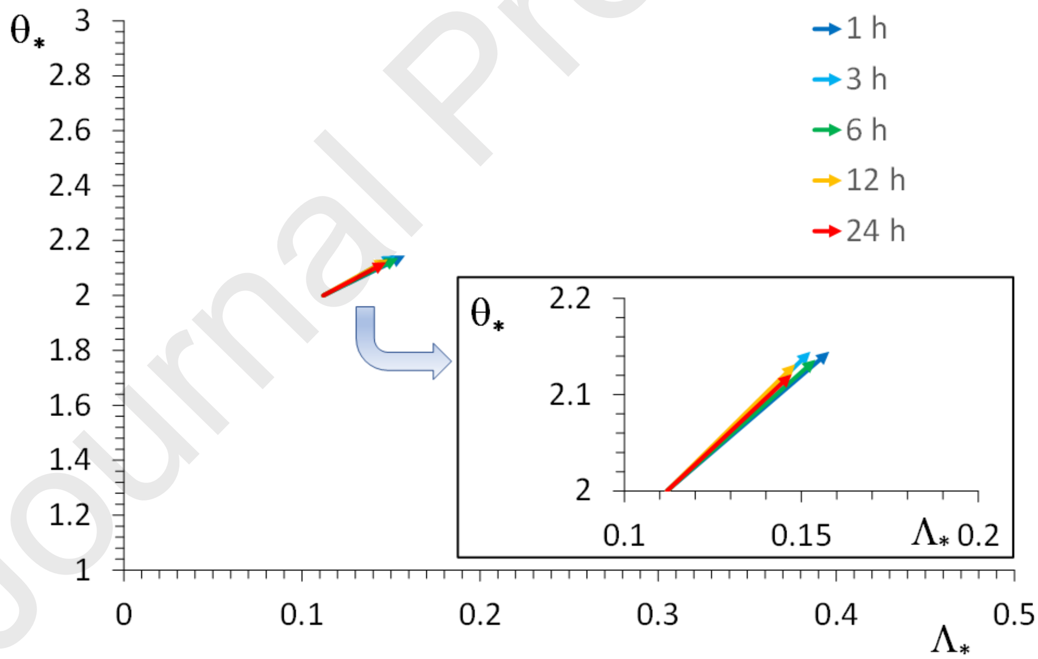

Figure 23. Vectors of variation on the plot (Λ_*, θ_*) for the TCEV parametric groups G_{2b}

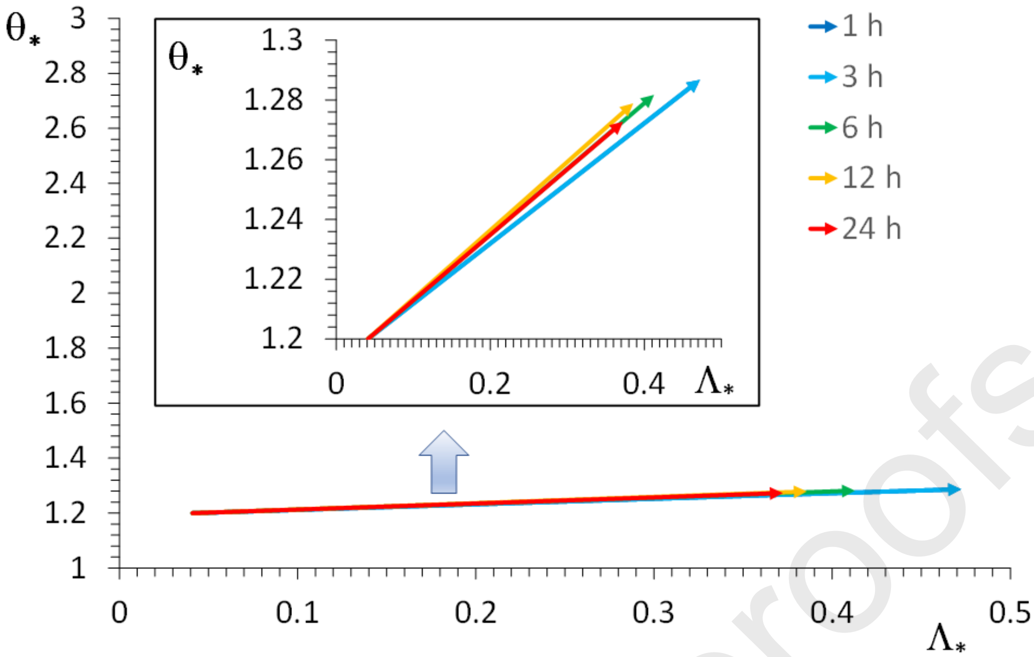

Figure 24. Vectors of variation on the plot (Λ_*, θ_*) for the TCEV parametric groups G_{2c}; according to Figs.12-13, θ_* very close to 1 induces significant increases for Λ_*, in order to respect prefixed change factors (from assumed climatic projections).

3.3. CC effects in terms of Hazard variation

Focusing on $d = 1$ h and on the groups $G_{1a,b,c}$ (the results for other scales and $G_{2a,b,c}$ are not shown but they are very similar), the plots of $\Delta H(x,t_1,t_2)$ (Eq. 25) concerning the assumed evolutions E1 (Fig. 15) and E2 (Fig. 16) are reported in Figs. 25-26, respectively. In detail: we set $t_2 - t_1 = 100$ years (as already mentioned in Sect. 3) and, regarding E2 evolution (Fig. 16), $t_* - t_1$ was fixed equal to 70 years (Caesar et al., 2013; Meinshausen et al., 2011; Rogelj et al., 2012; van Vuuren et al., 2011). Moreover, focusing on $\Lambda_1(t_1) = 15$, $\Lambda_2(t_1) = 0.5$ and $\theta_1(t_1) = 8$ mm, the cases $\theta_*(t_1) = 1.2$ (G_{1c}), $\theta_*(t_1) = 2$ (G_{1b}), $\theta_*(t_1) = 2.5$ (G_{1a}) and $\theta_*(t_1) = 3$ were analyzed.

For both types of evolution, $\theta_*(t_1) = 1.2$ induces the maximum peak of $\Delta H(.)$. This result can be explained by the following reason: as $\theta_*(t_1)$ values closer to 1 imply a marked increase of Λ_2 (see Sect. 3.1), i.e. the mean annual number of occurrences of outlier extreme events, it is clear that probability of having at least one exceedance of these rarer events (associated to $X_{0.99}(t_1)$, $X_{0.995}(t_1)$, and so on) in $(t_2 - t_1)$ years should much more increase if there is a strong growth for this frequency. Then, with the goal of having specific change factors for the quantiles of interest, the crucial role of initial skewness, and in particular of $\theta_*(t_1)$, emerges also for evaluation of $\Delta H(.)$.

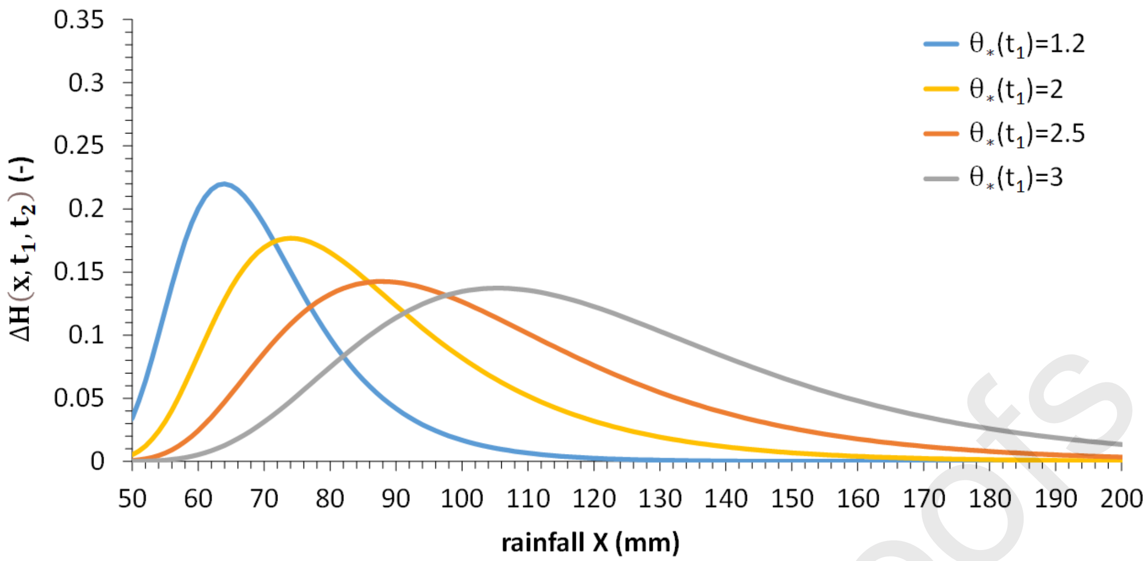

Figure 25. E1 evolution: plot of $\Delta H(x,t_1,t_2)$ for $\Lambda_1(t_1) = 15$, $\Lambda_2(t_1) = 0.5$ and $\theta_1(t_1) = 8$ mm and different $\theta_*(t_1)$

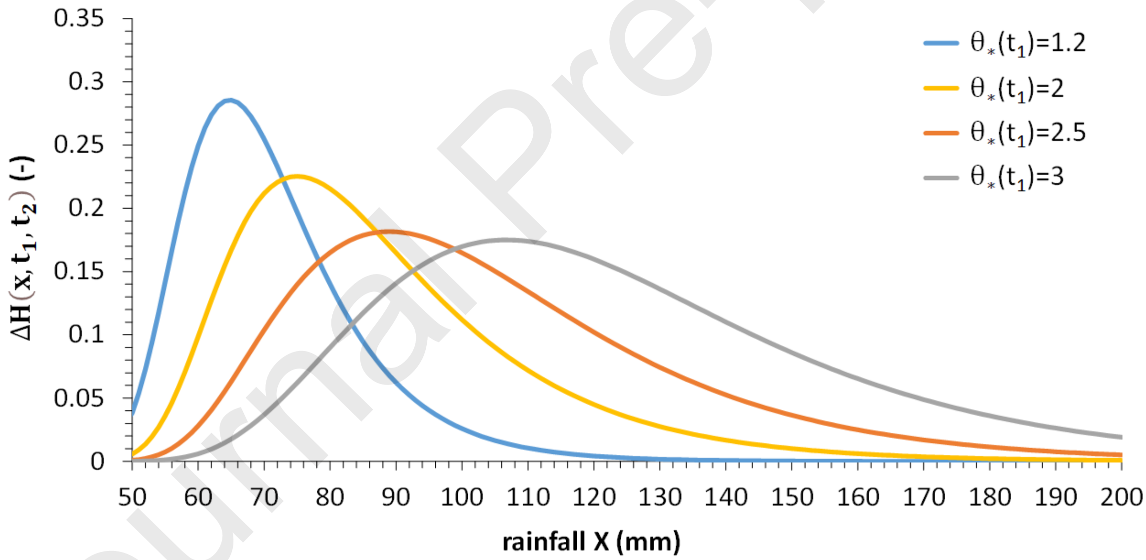

Figure 26. E2 evolution: plot of $\Delta H(x,t_1,t_2)$ for $\Lambda_1(t_1) = 15$, $\Lambda_2(t_1) = 0.5$ and $\theta_1(t_1) = 8$ mm and different $\theta_*(t_1)$

4. Conclusions

This work shows how CC effects can be quantified at hydrological resolutions with a quick and user-friendly methodology. Attention was focused on rainfall Annual Maxima (AM), and on how specific climate model projections, assumed as valid for the future horizons of interest, can be "assimilated" by the adopted probability distributions, used at rain gauge scale, i.e. point scale. In detail, after a discussion about GEV function, we analyzed in-depth the parametric space of TCEV distribution, particularly able to discriminate ordinary and rarer extreme events. The obtained results remarked that prefixed change factors, specific of the quantiles of interest, can be obtained in different ways, strongly depending on the initial skewness of time series modelled with TCEV. AM series that are initially "EV1 alike" skewed will be characterized by a strong increase of the mean annual frequency of outliers, and these results are coherent with Papalexiou and Montanari (2019), who found an increase in frequency of heavy extreme events at daily resolution, usually less skewed than the hourly scales. Future developments of this analysis will regard: i) the definition of transient rainfall Amount-Duration-Frequency curves (ADFs), which constitute the most used input for the design of several water systems, and ii) resilience evaluation for hydraulic structures of interest, in order to plan possible structural or non-structural measures to cope with possible Climate Change. For all the discussed aspects, we believe that this work and its following perspectives can be a valuable contribution to quantification of CC Effects.

References

Abramowitz M., Stegun I. A., 1970. Handbook of mathematical functions, Dover, New York, NY.

Balakrishnan N., Leung M. Y., 1988. Means, variances and covariances of order statistics, BLUEs for the Type-I generalized logistic distribution, and some applications. Communications in Statistics Simulation and Computation, 17(1), 51-84.

Ball J., Basbister M., Nathan R., Weeks W., Weinmann E., Retallick M., Testoni I., 2019. Australian rainfall and runoff: A guide to flood estimation, 1526. Symonston, ACT, Australia: Commonwealth of Australia (Geoscience Australia).

Ban N., Schmidli J., Schär. C., 2014. Evaluation of the convection resolving regional climate modeling approach in decade-long simulations. J. Geophys. Res.: Atmos. 119 (13), 7889-7907. https://doi.org/10.1002/2014JD021478.

Ban N., Rajczak J., Schmidli J., Schär C., 2020. Analysis of Alpine precipitation extremes using generalized extreme value theory in convection-resolving climate simulations. Clim. Dyn. 55 (1), 61-75. https://doi.org/10.1007/s00382-018-4339-4.

Beran M.; Hosking J. R. M., Arnell, N. W., 1986. Comment on 'Two component extreme value distribution for flood frequency analysis, by Rossi et al.'. Water Resources Research, 22(2), 263-266.

Berg P., Moseley C., Haerter. J. O., 2013. Strong increase in convective precipitation in response to higher temperatures. Nat. Geosci. 6 (3), 181-185. https://doi.org/10.1038/ngeo1731.

Berg P., Christensen O. B., Klehmet K., Lenderink G., Olsson J., Teichmann C., Yang W., 2019. Summertime precipitation extremes in a EURO-CORDEX 0.11 ensemble at an hourly resolution. Nat. Hazards Earth Syst. Sci. 19 (4), 957-971. https://doi.org/10.5194/nhess-19-957-2019.

Berthou S., Kendon E. J., Chan S. C., Ban N., Leutwyler D., Schär C., Fosser G., 2020. Pan-European climate at convection-permitting scale: A model intercomparison study. Clim. Dyn. 55 (1), 35-59. https://doi.org/10.1007/s00382-018-4114-6.

Blenkinsop S., Fowler H. J., Barbero R., Chan S. C., Guerreiro S. B., Kendon E., Lenderink G., Lewis E., Li X., Westra S., Alexander L., Allan R. P., Berg P., Dunn R. J. H., Ekström M., Evans J. P., Holland G., Jones R., Kjellström E., Klein-Tank A., Lettenmaier D., Mishra V., Prein A. F., Sheffield J., Tye M. R., 2018. The INTENSE project: Using observations and models to understand the past, present and future of sub-daily rainfall extremes. Adv. Sci. Res. 15, 117-126. https://doi.org/10.5194/asr-15-117-2018.

Blöschl G., Hall J., Viglione A., Perdigao R., Parajka J. Merz, B., Lun D., Arheimer B., Aronica G., Bilibashi A., et al., 2019. Changing climate both increases and decreases European river floods. Nature, 573, 108-111.

Bobee B., 1975. The Log Pearson Type 3 Distribution and Its Application in Hydrology. Water Resour. Res., 11(5), 681-689.

Boni G., Parodi A., Rudari R., 2006. Extreme rainfall events: learning from raingauge time series. J. Hydrol., 327 (3-4), 304-314. https://doi.org/10.1016/j.jhydrol.2005.11.050.

Butcher J. B., Zi T., 2019. Efficient method for updating IDF curves to future climate projections. Preprint, submitted June 11, 2019. https://arxiv.org/abs/1906.04802.

Caesar J., Palin E., Liddicoat S., Lowe J., Burke E., Pardaens A., Sanderson M., Kahana R., 2013. Response of the HadGEM2 Earth System Model to Future Greenhouse Gas Emissions Pathways to the Year 2300. Journal of Climate, 26, 3275-3284. http://journals.ametsoc.org/doi/abs/10.1175/JCLI-D-12-00577.1.

Caporali E., Cavigli E., Petrucci A., 2008. The index rainfall in the regional frequency analysis of extreme events in Tuscany (Italy). Environmetrics, 19 (7), 714-724. https://doi.org/10.1002/env.949.

Chandra R., Saha U., Mujumdar P. P., 2015. Model and parameter uncertainty in IDF relationships under climate change. Adv. Water Resour. 79 (May), 127-139. https://doi.org/10.1016/j.advwatres.2015.02.011.

Coles S., 2001. An introduction to statistical modeling of extreme values. London: Springer-Verlag, 208 p.

Cooley D., 2013. Return periods and return levels under climate change. In: Chapter 4, A. AghaKouchak, et al., eds. Extremes in a changing climate: detection, analysis and uncertainty. Dordrecht: Springer Science + Business media.

CSA (Canadian Standards Association). 2019. Technical guide: Development, interpretation and use of rainfall intensity-duration-frequency (IDF) information: Guideline for Canadian water resources practitioners. Mississauga, ON, Canada: CSA.

De Luca D.L., Galasso L., 2018. Stationary and Non-Stationary Frameworks for Extreme Rainfall Time Series in Southern Italy. Water, 10, 1477. https://doi.org/10.3390/w10101477

De Luca D.L., Napolitano F., 2023. A user-friendly software for modelling extreme values: EXTRASTAR (EXTRemes Abacus for STAtistical Regionalization). Environ. Model. Softw., 161, 105622. https://doi.org/10.1016/j.envsoft.2023.105622.

De Michele C., 2019. Advances in Deriving the Exact Distribution of Maximum Annual Daily Precipitation. Water, 11, 2322. https://doi.org/10.3390/w11112322.

Desiato F., Lena F., Toreti A., 2007. SCIA: A system for a better knowledge of the Italian climate. Boll. Geofis. Teor. Appl., 48, 351–358.

Dey D. K., Yan J., 2016. Extreme Value Modeling and Risk Analysis. Methods and Applications. Edited By Dipak K. Dey, Jun Yan CRC press.

El Adlouni, S., Ouarda T. B. M. J., Zhang X., Roy R., Bobée B., 2007. Generalized maximum likelihood estimators for the nonstationary generalized extreme value model. Water Resources Research, 43 (3), 1–13. doi:10.1029/2005WR004545.

EPWDR (Engineering and Public Works Department of Riverview). 2011. Storm water design criteria manual for municipal services, 88. Riverview, NB, Canada: EPWDR.

Fadhel S., Rico-Ramirez M. A., Han D., 2017. Uncertainty of intensity-duration-frequency (IDF) curves due to varied climate baseline periods. J. Hydrol. 547 (Apr), 600-612. https://doi.org/10.1016/j.jhydrol.2017.02.013.

Ferro V., Porto P., 1999. Regional analysis of rainfall-depth-duration equation for south Italy. Journal of Hydrologic Engineering, 4 (4), 326-336.

Fluixá-Sanmartín J., Morales-Torres A., Escuder-Bueno I., Paredes-Arquiola J., 2019. Quantification of climate change impact on dam failure risk under hydrological scenarios: A case study from a Spanish dam. Nat. Hazards Earth Syst. Sci. 19 (10), 2117-2139. https://doi.org/10.5194/nhess-19-2117-2019.

Forestieri A., Arnone E., Blenkinsop S., Candela A., Fowler H., Noto L. V., 2018a. The impact of climate change on extreme precipitation in Sicily, Italy. Hydrol. Processes 32 (3), 332-348. https://doi.org/10.1002/hyp.11421.

Forestieri A., Lo Conti F., Blenkinsop S., Cannarozzo M., Fowler H. J., Noto L. V., 2018b. Regional frequency analysis of extreme rainfall in Sicily (Italy). Int. J. Climatol., 38, e698-e716, 10.1002/joc.5400.

Fowler H. J., Lenderink G., Prein A. F., Westra S., Allan R. P., Ban N., Barbero R., Berg P., Blenkinsop S., Do H. X., Guerreiro S., Haerter J. O., Kendon E. J., Lewis E., Schaer C., Sharma A., Villarini G., Wasko C., Zhan X., 2021. Anthropogenic intensification of short-duration rainfall extremes. Nat. Rev. Earth Environ. 2 (2), 107-122. https://doi.org/10.1038/s43017-020-00128-6.

Ganguli P., Coulibaly P., 2019. Assessment of future changes in intensity-duration-frequency curves for Southern Ontario using North American (NA)-CORDEX models with nonstationary methods. J. Hydrol.: Reg. Stud. 22 (Apr), 100587. https://doi.org/10.1016/j.ejrh.2018.12.007.

Ganguli P., Coulibaly P., 2017. Does Nonstationarity in Rainfall Require Nonstationary Intensity-Duration-Frequency Curves? Hydrol. Earth Syst. Sci. 21, 6461–6483.

Gumbel E. J., 1958. Statistics of Extremes. Columbia University Press, New York.

Gupta S. K., 2011. Modern Hydrology and Sustainable Water Development. Wiley Online Library. Print ISBN:9781405171243; Online ISBN:9781444323962. DOI:10.1002/9781444323962.

Hassanzadeh E., Nazemi A., Elshorbagy A., 2014. Quantile-Based Downscaling of Precipitation Using Genetic Programming: Application to IDF Curves in Saskatoon. J. Hydrol. Eng. 19, 943–955.

Hosking J. R. M., Wallis J. R., 1987. Parameter and quantile estimation for the Generalized Pareto Distribution, Technometrics, 29(3), 339-349.

Hosseinzadehtalaei P., Tabari H., and Willems P., 2018. Precipitation intensity-duration-frequency curves for central Belgium with an ensemble of EURO-CORDEX simulations, and associated uncertainties. Atmos. Res. 200 (Feb), 1-12. https://doi.org/10.1016/j.atmosres.2017.09.015.

Hosseinzadehtalaei P., Tabari H., Willems P., 2020. Climate change impact on short-duration extreme precipitation and intensity–duration–frequency curves over Europe. J. Hydrol. 590 (Nov), 125249. https://doi.org/10.1016/j.jhydrol.2020.125249.

Hov Ø., Cubasch U., Fischer E., Höppe P., Iversen T., Kvamstø N. G., Kundzewicz Z. W., Rezacova D., Rios D., Duarte Santos F., Schädler B., Veisz O., Zerefos C., Benestad R., Murlis J., Donat M., Leckebusch G. C., Ulbrich U., 2013, Extreme weather events in Europe: Preparing for climate change adaptation, Norwegian Meteorological Institute, Oslo, Norway.

Jenkinson A. F., 1955. The frequency distribution of the annual maximum (or minimum) values of meteorological elements, Q. J. R. Meteorol. Soc., 81(348), 158-171, doi:10.1002/qj.49708134804.

Johnson N. L., Kotz S., Balakrishnan N., 1994. Continuous Univariate Distributions, Volume 1, 2nd Edition. New York, John Wiley and Sons.

Kao S.C., Ganguly A.R., 2011. Intensity, Duration, and Frequency of Precipitation Extremes under 21st-Century Warming Scenarios. J. Geophys. Res. 116, 16119.

Kendon E. J., Roberts N. M., Senior C. A., Roberts M. J., 2012. Realism of rainfall in a very high-resolution regional climate model. J. Clim. 25 (17), 5791-5806. https://doi.org/10.1175/JCLI-D-11-00562.1.

Kendon E. J., Roberts N. M., Fowler H. J., Roberts M. J., Chan S. C., Senior C. A., 2014. Heavier summer downpours with climate change revealed by weather forecast resolution model. Nat. Clim. Change 4 (7), 570–576. https://doi.org/10.1038/nclimate2258.

Kendon E. J., Prein A. F., Senior C. A., Stirling A., 2021. Challenges and outlook for convection-permitting climate modelling. Philos. Trans. R. Soc. A 379 (2195), 20190547. https://doi.org/10.1098/rsta.2019.0547.

Khazaei M. R. 2021. A robust method to develop future rainfall IDF curves under climate change condition in two major basins of Iran. Theor. Appl. Climatol. 144 (1), 179-190. https://doi.org/10.1007/s00704-021-03540-0.

Kilsby C. G., Jones, P. D., Burton A., Ford A. C., Fowler H. J., Harpham C., James P., Smith A., Wilby R. L., 2007. A daily weather generator for use in climate change studies. Environ. Model. Softw. 22, 1705-1719.

Kottegoda N. T., Rosso R., 2008. Applied Statistics for Civil and Environmental Engineers. Blackwell, Oxford, UK.

Kourtis I. M., Tsihrintzis V. A., 2022. Update of intensity-duration-frequency (IDF) curves under climate change: a review. Water Supply, 22 (5), 4951-4974. doi: https://doi.org/10.2166/ws.2022.152.

Kourtis I. M., Tsihrintzis V. A., 2021. Adaptation of urban drainage networks to climate change: A review. Sci. Total Environ., 771, 145431, 10.1016/j.scitotenv.2021.145431.

Kuo C.C., Gan T.Y., Gizaw M., 2015. Potential Impact of Climate Change on Intensity Duration Frequency Curves of Central Alberta. Clim. Chang. 130, 115–129.

Lanciotti S., Ridolfi E., Russo F., Napolitano F., 2022. Intensity-Duration-Frequency Curves in a Data-Rich Era: A Review. Water, 14, 3705. https://doi.org/10.3390/w14223705.

Lima C. H. R., Kwon H.-H., Kim J.-Y. 2016. A Bayesian beta distribution model for estimating rainfall IDF curves in a changing climate. J. Hydrol. 540 (Sep), 744-756. https://doi.org/10.1016/j.jhydrol.2016.06.062.

Lombardo F., Napolitano F., Russo F., Koutsoyiannis D. (2019). On the exact distribution of correlated extremes in hydrology. Water Resour. Res., 55, 10405-10423.

Madsen H., Lawrence D., Lang M., Martinkova M., Kjeldsen T. R., 2014. Review of trend analysis and climate change projections of extreme precipitation and floods in Europe. J. Hydrol. 519 (Nov), 3634-3650. https://doi.org/10.1016/j.jhydrol.2014.11.003.

Mailhot A., Duchesne S., Caya D., Talbot G., 2007. Assessment of Future Change in Intensity–Duration–Frequency (IDF) Curves for Southern Quebec Using the Canadian Regional Climate Model (CRCM). J. Hydrol. 347, 197–210.

Mantegna G. A., White C. J., Remenyi T. A., Corney S. P., Fox-Hughes P., 2017. Simulating sub-daily intensity-frequency-duration curves in Australia using a dynamical high-resolution regional climate model. J. Hydrol. 554 (Nov), 277-291. https://doi.org/10.1016/j.jhydrol.2017.09.025.

Marani M., Ignaccolo M., 2015. A metastatistical approach to rainfall extremes. Adv. Water Resour., 79, 121-126.

Martel J.-L., Brissette F., Lucas-Picher P., Troin M., Arsenault R., 2021. Climate change and rainfall intensity-duration-frequency (IDF) curves: Overview of science and guidelines for adaptation. Journal of Hydrologic Engineering. https://doi.org/10.1061/(ASCE)HE.1943-5584.0002122.

Mazzoglio P., Butera I., Claps P., 2020. I2-RED: A Massive Update and Quality Control of the Italian Annual Extreme Rainfall Dataset, Water 12 (12): 3308. https://doi.org/10.3390/w12123308

MDDELCC (Ministère du Développement durable, de l'Environnement et de la Lutte contre les changements climatiques), 2017. Manuel de calcul et de conception des ouvrages municipaux de gestion des eaux pluviales, 125. [In French.] Québec: MDDELCC.

Meinshausen M., Smith S. J., Calvin K J., Daniel S., Kainuma M. L. T., Lamarque J-F., Matsumoto K., Montzka S. A., Raper S. C. B., Riahi K., Thomson A., Velders G. J. M., van Vuuren D.P. P., 2011. The RCP greenhouse gas concentrations and their extensions from 1765 to 2300. Climatic Change 109, 213. http://link.springer.com/article/10.1007/s10584-011-0156-z.

Mirhosseini G., Srivastava P., Stefanova L., 2013. The Impact of Climate Change on Rainfall Intensity-Duration-Frequency (IDF) Curves in Alabama. Reg. Environ. Change. 13, 25–33.

Moccia B., Papalexiou S. M., Russo F., Napolitano F., 2021. Spatial variability of precipitation extremes over Italy using a fine-resolution gridded product. J. Hydrol.: Regional Studies, 37, 100906. https://doi.org/10.1016/j.ejrh.2021.100906.

Nazarenko L., Schmidt G. A., Miller R. L., Tausnev N., Kelley M., Ruedy R., Russell G. L., Aleinov I., Bauer M., Bauer S., Bleck R., Canuto V., Cheng Y., Clune T. L., Del Genio A. D., Faluvegi G., Hansen J. E., Healy R. J., Kiang N. Y., Koch D., Lacis A. A., LeGrande A. N., Lerner J., Lo K. K., Menon S., Oinas V., Perlwitz J., Puma M. J., Rind D., Romanou A., Sato M., Shindell D. T., Sun S., Tsigaridis K., Unger N., Voulgarakis A., Yao M.-S., Zhang J., 2015. Future climate change under RCP emission scenarios with GISS ModelE2. J. Adv. Model. Earth Syst. 7, 244-267. https://doi.org/10.1002/2014MS000403.

Onof C., Arnbjerg-Nielsen K, 2009. Quantification of anticipated future changes in high resolution design rainfall for urban areas. Atmos. Res., 92, 350-363.

Pan X., Rahman A., Haddad K., Ouarda T. B. M. J., 2022. Peaks-over-threshold model in flood frequency analysis: a scoping review. Stoch Environ Res Risk Assess 36, 2419-2435. https://doi.org/10.1007/s00477-022-02174-6.

Papalexiou S. M., Montanari A., 2019. Global and Regional Increase of Precipitation Extremes Under Global Warming. Water Resour. Res., 55(6), 4901-4914, 10.1029/2018WR024067.

Parey S., Malek F., Laurent C., Dacunha-Castelle D., 2007. Trends and climate evolution: statistical approach for very high temperatures in France. Climatic Change, 81 (3–4), 331-352. doi:10.1007/s10584-006-9116-4.

Parey S., Hoang T.T.H., Dacunha-Castelle, D., 2010. Different ways to compute temperature return levels in the climate change context. Environmetrics, 21, 698-718. https://doi.org/10.1002/env.1060.

Press W. H., Flannery B. P., Teukolsky S. A., Vetterling, W. T., 1988. Numerical Recipes in C. The art of scientific computing, Cambridge University Press,.

Ragno E., AghaKouchak A., Love C. A., Cheng L., Vahedifard F., Lima C. H. R., 2018. Quantifying changes in future intensity-duration-frequency curves using multimodel ensemble simulations. Water Resour. Res. 54 (3),1751-1764. https://doi.org/10.1002/2017WR021975.

Rogelj J., Meinshausen M., Knutti R., 2012. Global warming under old and new scenarios using IPCC climate sensitivity range estimates. Nature Climate Change 2, 248-253. http://www.nature.com/nclimate/journal/v2/n4/full/nclimate1385.html.

Rossi F.; Fiorentino M., Versace P., 1984. Two-component extreme value distribution for flood frequency analysis. Water Resour. Res., 20, 847-856.

Ruggiero P., Komar P. D., Allan, J. C., 2010. Increasing wave heights and extreme value projections: the wave climate of the U.S. Pacific Northwest. Coastal Engineering, 57 (5), 539-552. doi:10.1016/j.coastaleng.2009.12.005.

Salas J. D., Obeysekera J., 2014. Revisiting the Concepts of Return Period and Risk for Nonstationary Hydrologic Extreme Events. J. Hydrol. Eng., 19, 554-568.

Salas J. D., Obeysekera J., Vogel R. M., 2018. Techniques for assessing water infrastructure for nonstationary extreme events: a review, Hydrological Sciences Journal, 63:3, 325-352, doi:10.1080/02626667.2018.1426858.

Sandink D., Simonovic S.P., Schardong A., Srivastav R., 2016. A Decision Support System for Updating and Incorporating Climate Change Impacts into Rainfall Intensity-Duration-Frequency Curves: Review of the Stakeholder Involvement Process. Environ. Model. Softw., 84, 193–209.

Seneviratne S. I., Nicholls N., Easterling D., Goodess C. M., Kanae S., Kossin J., Luo Y., Marengo J., McInnes K., Rahimi M., Reichstein M., Sorteberg A., Vera C., Zhang, X., 2012, Changes in climate extremes and their impacts on the natural physical environment, in: Managing the risks of extreme events and disasters to advance climate change adaptation, Cambridge University Press, Cambridge, United Kingdom, 109-230.

Shahabul Alam M., Elshorbagy A., 2015. Quantification of the Climate Change-Induced Variations in Intensity–Duration–Frequency Curves in the Canadian Prairies. J. Hydrol. 527, 990–1005.

Simonovic S.P., Schardong A., Sandink D., Srivastav R., 2016. A Web-Based Tool for the Development of Intensity Duration Frequency Curves under Changing Climate. Environ. Model. Softw. 81, 136–153.

Singh V. P., 1998. Entropy-based parameter estimation in hydrology. Springer Netherlands, Dordrecht.

Srivastav R. K., Schardong A., Simonovic S. P., 2014. Equidistance quantile matching method for updating IDF curves under climate change. Water Resour. Manage. 28 (9), 2539-2562. https://doi.org/10.1007/s11269-014-0626-y.

Svenskt Vatten, 2011. Nederbördsdata vid dimensionering och analys av avloppssystem (Rain Data for Design and Analysis of Urban Drainage Systems). [In Swedish.] Publikation P104. Stockholm, Sweden: Svenskt Vatten.

Themeßl M. J., Gobiet A., Heinrich G. 2012 Empirical-statistical downscaling and error correction of regional climate models and its impact on the climate change signal. Clim. Change 112, 449-468. https://doi.org/10.1007/s10584-011-0224-4.

Todorovic P., 1970. On Some Problems Involving Random Number of Random Variables. Ann. Math. Stat., 41(3), 1059-1063.

van Vuuren D. P., Edmonds J., Kainuma M., Riahi K., Thomson A., Hibbard K., Hurtt G. C., Kram T., Krey V., Lamarque J.-F., Masui T., Meinshausen M., Nakicenovic N., Smith S. J., Rose S. K., 2011. The representative concentration pathways: an overview. Climatic Change 109, 5. http://link.springer.com/article/10.1007/s10584-011-0148-z%20/fulltext.html.

Vergara-Temprado J., Ban N., Schär C., 2021. Extreme sub-hourly precipitation intensities scale close to the Clausius-Clapeyron rate over Europe. Geophys. Res. Lett. 48 (3), e2020GL089506. https://doi.org/10.1029/2020GL089506.

Versace P., Ferrari E., Gabriele S., Rossi, F., 1989.Valutazione delle Piene in Calabria (CNR-IRPI e GNDCI: Geodata, Cosenza, Italy). In Italian.

Volpi E., 2019. On return period and probability of failure in hydrology. WIREs Water. 6, e1340. https://doi.org/10.1002/wat2.1340.

Westra S., Fowler H. J., Evans J. P., Alexander L. V., Berg P., Johnson F., Kendon E. J., Lenderink G., Roberts N. M., 2014. Future changes to the intensity and frequency of short-duration extreme rainfall. Rev. Geophys. 52 (3), 522-555. https://doi.org/10.1002/2014RG000464.

Willems P., 2011. Revision of urban drainage design rules based on extrapolation of design rainfall statistics. In Proc., 12th Int. Conf. on Urban Drainage. London: International Water Association.

Figure 1. Plot of Change Factor $C(F)$, specific for any investigated cell and sub-daily duration (adapted from Hosseinzadehtalaei et al., 2020)

Figure 2. Overview of the proposed methodology.

Figure 3. Examples of GEV functions for specific b values on the EV1 probabilistic plot. The slope angle $\text{arctg}\,(1/\theta)$ and the intercept $-\ln\Lambda$ are related to the straight line associated to EV1 function, i.e. a GEV with $b = 0$.

Figure 4. GEV skewness against the shape parameter b.

Figure 5. $\Delta X_F/X_F$ for several initial values of Λ and $F = 0.5, 0.9$, when $b = 0$ (EV1) and $b = -0.1$ and -0.2 (EV2), and by considering $M = 1, 1.2, 1.3$ and K varying from 0.5 to 3.

Figure 6. $\Delta X_F/X_F$ for several initial values of Λ and $F = 0.98, 0.995$, when $b = 0$ (EV1) and $b = -0.1$ and -0.2 (EV2), and by considering $M = 1, 1.2, 1.3$ and K varying from 0.5 to 3.

Figure 7. EV1 probabilistic plot. Qualitative example of TCEV (green) curve, and ordinary (straight blue line) and outlier (straight red line) components.

Figure 8. Scenario 1 for NS-TCEV, on EV1 probabilistic plot.

Figure 9. Scenario 2 for NS-TCEV, on EV1 probabilistic plot.

Figure 10. Scenario 3 for NS-TCEV, on EV1 probabilistic plot.

Figure 11. Scenario 4 for NS-TCEV, on EV1 probabilistic plot.

Figure 12. Plot of $Y_{0.98}(\theta_*,\Lambda_*)$, from which it is possible to quantify the variations of quantile Y_F on the basis on $\Delta\theta_*(t_2-t_1)=\theta_*(t_2)-\theta_*(t_1)$ and $\Delta\Lambda_*(t_2-t_1)=\Lambda_*(t_2)-\Lambda_*(t_1)$; it is clear that, for $\theta_*(t_1)$ and $\theta_*(t_2)$ very close to 1, the increases of Y_F are not relevant even for a significant growth of Λ_*.

Figure 13. Plot of $Y_{0.995}(\theta_*,\Lambda_*)$, from which it is possible to quantify the variations of quantile Y_F on the basis on $\Delta\theta_*(t_2-t_1)=\theta_*(t_2)-\theta_*(t_1)$ and $\Delta\Lambda_*(t_2-t_1)=\Lambda_*(t_2)-\Lambda_*(t_1)$; it is clear that, for $\theta_*(t_1)$ and $\theta_*(t_2)$ very close to 1, the increases of Y_F are not relevant even for a significant growth of Λ_*.

Figure 14. Plot of Y_F and $\partial Y_F/\partial\Lambda_*$ depending on Λ_*, for fixed values of θ_*; according to Figs.12-13, θ_* very close to 1 induces (mainly for higher F) smaller variations of Y_F, whatever is the value of Λ_*.

Figure 15. E1 temporal evolution for the function $\Lambda_1(t)$, $\theta_1(t)$, $\Lambda_2(t)$ and $\theta_2(t)$

Figure 16. E2 temporal evolution for the function $\Lambda_1(t)$, $\theta_1(t)$, $\Lambda_2(t)$ and $\theta_2(t)$

Figure 17. Estimation of K_1, K_2 for the TCEV parametric groups G_{1a}, G_{1b}, G_{1c}

Figure 18. Estimation of K_1, K_2 for the TCEV parametric groups G_{2a}, G_{2b}, G_{2c}

Figure 19. Vectors of variation on the plot (Λ_*, θ_*) for the TCEV parametric groups G_{1a}

Figure 20. Vectors of variation on the plot (Λ_*, θ_*) for the TCEV parametric groups G_{1b}

Figure 21. Vectors of variation on the plot (Λ_*, θ_*) for the TCEV parametric groups G_{1c}

Figure 22. Vectors of variation on the plot (Λ_*, θ_*) for the TCEV parametric groups G_{2a}

Figure 23. Vectors of variation on the plot (Λ_*, θ_*) for the TCEV parametric groups G_{2b}

Figure 24. Vectors of variation on the plot (Λ_*, θ_*) for the TCEV parametric groups G_{2c}; according to Figs.12-13, θ_* very close to 1 induces significant increases for Λ_*, in order to respect prefixed change factors (from assumed climatic projections).

Figure 25. E1 evolution: plot of $\Delta H(x,t_1,t_2)$ for $\Lambda_1(t_1)=15$, $\Lambda_2(t_1)=0.5$ and $\theta_1(t_1)=8$ mm and different $\theta_*(t_1)$

Figure 26. E2 evolution: plot of $\Delta H(x,t_1,t_2)$ for $\Lambda_1(t_1)=15$, $\Lambda_2(t_1)=0.5$ and $\theta_1(t_1)=8$ mm and different $\theta_*(t_1)$